Spatiotemporal evolution of focused single-cycle electromagnetic pulses

Simin Feng and Herbert G. Winful
Department of Electrical Engineering and Computer Science, University of Michigan, 1301 Beal Avenue, Ann Arbor, Michigan 48109-2122

Robert W. Hellwarth
Department of Physics and Department of Electrical Engineering, University of Southern California, Los Angeles, California 90089-0484

(Received 7 August 1998)

We analyze exact solutions of Maxwell's equations that are capable of describing focused single-cycle electromagnetic pulses. These finite energy solutions are a subset of Ziolkowski's ''modified power spectrum'' pulse solutions [Phys. Rev A **39**, 2005 (1989)]. They display substantial temporal reshaping, time reversal, and polarity reversals as they pass through the focus. The temporal profiles at the focus and in the far field are related by a Hilbert transform in time. These results are explained in terms of the Gouy phase shift of focused beams. We also show that these pulse solutions are natural spatiotemporal modes of an open resonator and propose methods for their practical realization. [S1063-651X(99)06304-7]

PACS number(s): 41.20.Jb, 42.60.Da, 42.25.Bs

I. INTRODUCTION

There is much current interest in exact pulse solutions of Maxwell's equations that describe the localized transmission of electromagnetic energy in free space [1–4]. These studies were initiated by Brittingham [1] who introduced the so-called ''focus wave modes'' (FWM's), which are three-dimensional packetlike solutions of the homogeneous Maxwell's equations. The original FWM's had finite energy density but infinite total energy and hence were physically unrealizable. In a major advance, Ziolkowski obtained finite energy solutions he termed ''electromagnetic directed energy pulse trains'' (EDEPT's) by forming appropriate superpositions of the focus wave modes [2,3]. Hellwarth and Nouchi have recently explored a particular subset of these EDEPT's and obtained solutions that depict single-cycle electromagnetic pulses the fields of which are confined to toroidal wave packets and thus resemble focused doughnuts [4]. In that work and in Ref. [3], the vector electromagnetic field components were derived from a complex Hertz potential $\hat{z}f(\mathbf{r},t)$ oriented in the direction of wave propagation. The real and imaginary parts of the scalar generating function $f(\mathbf{r},t)$ are solutions of the scalar wave equation in vacuum. They respectively lead to the long pulse ($1\frac{1}{2}$-cycle) and short pulse (one-cycle) solutions described in Ref. [4].

A number of open questions were posed by Hellwarth and Nouchi regarding these focused one-cycle electromagnetic pulse solutions of Maxwell's equations. In particular, it is not known what kind of electromagnetic fields are produced with a Hertz vector oriented transverse to the direction of propagation. It is also of interest to know if there is a simple transformation that relates the long pulse solution to the short pulse solution. Finally, there is the question of the practical realization of these pulse solutions in the laboratory.

In this paper we provide the exact electromagnetic field solutions of Maxwell's equations for a transversely oriented (along x) Hertz vector [5]. We find that the resulting fields are oblate wave packets that resemble ''focused pancakes.'' We carry out an explicit calculation that yields the finite total energy contained in these pulses. The real and imaginary pulse solutions are shown to be related by a Hilbert transform in time at any position $\mathbf{r}$. In fact, we find that the real and imaginary solutions transform into one another as the pulses propagate from the focus to the far field. The near-field and far-field temporal profiles are thus related by a Hilbert transform. We also show how the well known Gouy shift of focused beams leads to polarity reversals, time reversal, and temporal reshaping as the pulses evolve through the focus. The properties of the pulse solutions are completely determined by two parameters: q_1, which is related to the peak wavelength, and q_2, which determines the Rayleigh length. In the limit $q_1 \ll q_2$, which corresponds to the paraxial regime, a number of useful approximate relations are obtained. The results are applied to recent observations on single-cycle terahertz electromagnetic pulses [6]. We demonstrate that these paraxial solutions are the natural spatiotemporal modes of an open electromagnetic cavity. This leads to the idea that EDEPT's can be generated in the laboratory by exciting a curved mirror resonator or by propagation along a lens waveguide.

II. DERIVATION OF FIELDS

Our analysis is based on exact solutions of the wave equation of the type developed by Ziolkowski to describe efficient, localized transmission of electromagnetic energy in space-time. The free-space propagation of electromagnetic pulses is governed by the wave equation

$$\left\{\nabla^2 - \frac{1}{c^2}\frac{\partial^2}{\partial t^2}\right\} f(\mathbf{r},t) = 0, \tag{2.1}$$

where $f(\mathbf{r},t)$ is a scalar function. A particularly useful exact solution of this equation is the modified Gaussian pulse [3],

$$G_k(\mathbf{r},t)=\frac{\exp\{-k\rho^2/(q_1+i\tau)\}}{(q_1+i\tau)}\exp\{ik(z+ct)\}, \quad (2.2)$$

where $\rho=(x^2+y^2)^{1/2}$ is the transverse coordinate, z is the propagation direction, $\tau=z-ct$, k is a constant with dimensions $(\text{length})^{-1}$, and q_1 is a positive parameter with dimensions of length. These solutions have finite energy density but infinite total energy and hence do not adequately represent a physical space-time localized pulse. They can nevertheless be used as basis functions to synthesize finite energy pulse solutions through the superposition

$$f(\mathbf{r},t)=\int_0^{+\infty} dk\, G_k(\mathbf{r},t)F(k), \quad (2.3)$$

where $F(k)$ is a weighting function that satisfies certain general square-integrability conditions [3]. A physically motivated choice of the k spectrum is

$$F(k)=\begin{cases} f_0\exp(-kq_2), & k>0, \\ 0, & k\leqslant 0, \end{cases} \quad (2.4)$$

which reminds one of the Boltzmann factor governing the probability of exciting a particular Gaussian mode of energy proportional to k. Here q_2 is a positive parameter. With use of Eqs. (2.4) and (2.2) in Eq. (2.3), we obtain the scalar generating function

$$f(\mathbf{r},t)=\frac{f_0}{\rho^2+(q_1+i\tau)(q_2-i\sigma)}, \quad (2.5)$$

where $\sigma\equiv z+ct$. In Sec. IV F, it will be shown that the parameters q_1 and q_2 characterize, respectively, the effective wavelength and Rayleigh range of the pulses. All the physical properties of the solutions, such as pulse width, spectral width, and far-field diffraction angle, are completely determined by these two parameters. The function $f(\mathbf{r},t)$ expressed by Eq. (2.5) has finite energy and is an exact solution of the scalar wave equation.

Solutions to Maxwell's equations are found from this generating function by constructing a Hertz vector oriented, for example, along a transverse direction:

$$\mathbf{\Pi}=\hat{\mathbf{x}}f(\mathbf{r},t), \quad (2.6)$$

where $\hat{\mathbf{x}}$ is a unit vector, and $f(\mathbf{r},t)$ is the generating function given by Eq. (2.5). (In previous work [4], use of a z-directed Hertz vector resulted in toroidal, focused doughnut wave packets.) The vector electromagnetic field components are then found from

$$\mathbf{E}(\mathbf{r},t)=-\mu_0\frac{\partial}{\partial t}(\nabla\times\mathbf{\Pi}),$$
$$\mathbf{H}(\mathbf{r},t)=\nabla\times(\nabla\times\mathbf{\Pi}), \quad (2.7)$$

since the electromagnetic scalar potential is zero. Using Maxwell's equations, these relations can be written as

$$\mathbf{E}=\hat{\mathbf{y}}\left\{-\mu_0\frac{\partial}{\partial z}\left(\frac{\partial f}{\partial t}\right)\right\}+\hat{\mathbf{z}}\left\{\mu_0\frac{\partial}{\partial y}\left(\frac{\partial f}{\partial t}\right)\right\}, \quad (2.8)$$

$$\mathbf{H}=\hat{\mathbf{x}}\left\{\frac{\partial^2 f}{\partial x^2}-\frac{1}{c^2}\frac{\partial^2 f}{\partial t^2}\right\}+\hat{\mathbf{y}}\frac{\partial^2 f}{\partial y\,\partial x}+\hat{\mathbf{z}}\frac{\partial^2 f}{\partial z\,\partial x}, \quad (2.9)$$

where $\hat{\mathbf{x}}$, $\hat{\mathbf{y}}$, and $\hat{\mathbf{z}}$ are unit vectors along the corresponding axes, and c is the light velocity in vacuum. The electric field along the x direction is exactly zero due to the x orientation of the Hertz vector. Using Eq. (2.5) in Eqs. (2.8) and (2.9), we obtain the following components of the electromagnetic field:

$$E_y(\mathbf{r},t)=2f_0\sqrt{\frac{\mu_0}{\varepsilon_0}}\frac{(q_1+i\tau)^2-(q_2-i\sigma)^2}{\{\rho^2+(q_1+i\tau)(q_2-i\sigma)\}^3}, \quad (2.10)$$

$$E_z(\mathbf{r},t)=-i4f_0\sqrt{\frac{\mu_0}{\varepsilon_0}}\frac{(q_1+i\tau)+(q_2-i\sigma)}{\{\rho^2+(q_1+i\tau)(q_2-i\sigma)\}^3}\rho\sin\varphi, \quad (2.11)$$

$$H_x(\mathbf{r},t)=2f_0\frac{2\rho^2\cos(2\varphi)+(q_1+i\tau)^2+(q_2-i\sigma)^2}{\{\rho^2+(q_1+i\tau)(q_2-i\sigma)\}^3}, \quad (2.12)$$

$$H_y(\mathbf{r},t)=4f_0\frac{\rho^2\sin(2\varphi)}{\{\rho^2+(q_1+i\tau)(q_2-i\sigma)\}^3}, \quad (2.13)$$

$$H_z(\mathbf{r},t)=i4f_0\frac{(q_2-i\sigma)-(q_1+i\tau)}{\{\rho^2+(q_1+i\tau)(q_2-i\sigma)\}^3}\rho\cos\varphi, \quad (2.14)$$

where ε_0 is the permittivity of the vacuum, and $\varphi=\tan^{-1}(y/x)$ is the azimuthal angle. Eqs. (2.10)–(2.14) are exact solutions of Maxwell's equations. Due to the linearity and reality of the wave equation and Maxwell's equations, the real and the imaginary parts of the fields constitute two physical pulse solutions. They originate separately from the real and the imaginary parts of the generating function. For $q_1\leqslant q_2$ both the real and the imaginary solutions represent focused single-cycle pulses propagating in free space with the energy confined near the propagation axis. By duality we can obtain another set of solutions $(\mathbf{E}',\mathbf{H}')$ by letting $\mathbf{E}'=\sqrt{\mu_0/\varepsilon_0}\mathbf{H}$ and $\mathbf{H}'=-\sqrt{\varepsilon_0/\mu_0}\mathbf{E}$.

A. Analyticity of pulse solutions

An important property of the electromagnetic field solutions Eqs. (2.10)–(2.14) as well as the generating function Eq. (2.5) is that they are analytic functions of time at any position $\mathbf{r}$. This means that their poles lie in the lower half of the complex plane regardless of the values of ρ and z. These poles are the solutions of the quadratic equation

$$\rho^2+(q_1+i\tau)(q_2-i\sigma)=0,$$

and are given by

$$ct_1 = -i\frac{q_2+q_1}{2} - \sqrt{\left(z+i\frac{q_2-q_1}{2}\right)^2+\rho^2}$$

$$ct_2 = -i\frac{q_2+q_1}{2} + \sqrt{\left(z+i\frac{q_2-q_1}{2}\right)^2+\rho^2}. \quad (2.15)$$

It is shown in Appendix A that the imaginary parts of these roots are always negative and hence the field solutions are analytic functions of time.

B. Hilbert transform relationship

Since the field solutions and the generating function are analytic functions of time, their real and imaginary parts are Hilbert transforms of each other. For the electric field we have

$$\mathbf{E}_r(\mathbf{r},t) = -\frac{1}{\pi}\mathrm{P}\int_{-\infty}^{+\infty}\frac{\mathbf{E}_i(\mathbf{r},t')}{t-t'}dt',$$

$$\mathbf{E}_i(\mathbf{r},t) = \frac{1}{\pi}\mathrm{P}\int_{-\infty}^{+\infty}\frac{\mathbf{E}_r(\mathbf{r},t')}{t-t'}dt', \quad (2.16)$$

where $\mathbf{E}_r$ and $\mathbf{E}_i$ are the real and imaginary parts of the electric field given in Eqs. (2.10)–(2.14) and P stands for principal value. This transform relationship simplifies in the frequency domain. Define the Fourier transform pair

$$\tilde{\mathbf{E}}(\mathbf{r},\omega) = \int_{-\infty}^{+\infty}\mathbf{E}(\mathbf{r},t)\exp(-i\omega t)dt,$$

$$\mathbf{E}(\mathbf{r},t) = \frac{1}{2\pi}\int_{-\infty}^{+\infty}\tilde{\mathbf{E}}(\mathbf{r},\omega)\exp(i\omega t)d\omega. \quad (2.17)$$

Then the Hilbert transform relationship between the real and imaginary parts of $\mathbf{E}(\mathbf{r},t)$ in the frequency domain can be expressed as

$$\tilde{\mathbf{E}}_r(\mathbf{r},\omega) = i\,\mathrm{sgn}(\omega)\tilde{\mathbf{E}}_i(\mathbf{r},\omega),$$

$$\tilde{\mathbf{E}}_i(\mathbf{r},\omega) = -i\,\mathrm{sgn}(\omega)\tilde{\mathbf{E}}_r(\mathbf{r},\omega), \quad (2.18)$$

where

$$\mathrm{sgn}(\omega) = \begin{cases} 1, & \text{if } \omega>0, \\ 0, & \text{if } \omega=0, \\ -1, & \text{if } \omega<0. \end{cases}$$

C. Orthogonality of pulse solutions

The real and the imaginary solutions form two spatiotemporal modes of single-cycle pulses. This point will become clearer after we discuss the physical properties of these solutions. The two modes are orthogonal at any space point $\mathbf{r}$, i.e.,

$$\int_{-\infty}^{+\infty}E_r(\mathbf{r},t)E_i(\mathbf{r},t)dt = 0. \quad (2.19)$$

To prove this we start with Parseval's equality,

$$\int_{-\infty}^{+\infty}E_r(\mathbf{r},t)E_i(\mathbf{r},t)dt = \frac{1}{2\pi}\int_{-\infty}^{+\infty}\tilde{E}_r(\mathbf{r},\omega)\tilde{E}_i^*(\mathbf{r},\omega)d\omega, \quad (2.20)$$

and use the Hilbert transform relationship, Eq. (2.18), and the fact that $E_r(\mathbf{r},t)$ and $E_i(\mathbf{r},t)$ are real.

III. ENERGY OF PULSE SOLUTIONS

If these pulse solutions are to be physically realizable, their energy content should be finite. In Ref. [3], Ziolkowski showed that for a longitudinally oriented Hertz vector, the EDEPT will have finite total energy if the spectrum $kF(k)$ is square integrable. In Appendix B, we will present a detailed calculation to show that for a transversely oriented Hertz vector the total energy of the EDEPT solution is given by

$$\begin{aligned} U_{\mathrm{EM}} &= \frac{1}{2}\int_{-\infty}^{+\infty}dz\int_0^{+\infty}\rho\,d\rho\int_0^{2\pi}d\varphi(\varepsilon_0|E_y|^2+\varepsilon_0|E_z|^2 \\ &\quad +\mu_0|H_x|^2+\mu_0|H_y|^2+\mu_0|H_z|^2) \\ &= \frac{3\pi^2\mu_0}{4q_1^4}\int_0^{+\infty}dk|F(k)|^2 \\ &\quad \times[1+\tfrac{2}{3}(kq_1)+\tfrac{2}{3}(kq_1)^2+\tfrac{4}{3}(kq_1)^3] \\ &= U_r+U_i, \end{aligned} \quad (3.1)$$

where U_r and U_i represent, respectively, the energy of the real and the imaginary pulses. Thus for a transverse orientation of the Hertz vector an EDEPT will have finite energy if the spectrum $k^{3/2}F(k)$ is square integrable.

With the particular spectrum $F(k)$ given by Eq. (2.4), the generating function, Eq. (2.5), as well as the field components Eqs. (2.10)–(2.14) are analytic functions of time at any spatial point $\mathbf{r}$. This property can be used with the wave equation to show that the real and the imaginary solutions have equal amounts of electric energy and magnetic energy. Hence, the total energy of the real pulse equals that of the imaginary pulse. Note that both real and imaginary solutions satisfy the wave equation. Taking the Fourier transform (with respect to time) of the wave equation, we have

$$\nabla^2\tilde{\mathbf{E}}_{r,i}(\mathbf{r},\omega) = -\frac{\omega^2}{c^2}\tilde{\mathbf{E}}_{r,i}(\mathbf{r},\omega), \quad (3.2)$$

where r and i refer to the real and imaginary solutions, respectively. Equation (3.2) implies that vectors $\tilde{\mathbf{E}}_{r,i}(\mathbf{r},\omega)$ are the eigenfunctions of the Hermitian operator ∇^2, corresponding to the eigenvalue $-\omega^2/c^2$. Therefore, the following orthogonality relations hold:

$$\int\int\int\tilde{\mathbf{E}}_r^*(\mathbf{r},\omega)\cdot\tilde{\mathbf{E}}_r(\mathbf{r},\omega')d\mathbf{r} = S_r(\omega)\delta(\omega'-\omega),$$

$$\int\int\int\tilde{\mathbf{E}}_i^*(\mathbf{r},\omega)\cdot\tilde{\mathbf{E}}_i(\mathbf{r},\omega')d\mathbf{r} = S_i(\omega)\delta(\omega'-\omega). \quad (3.3)$$

Using Eq. (3.3), the electric energy of the pulse can be written as

$$U_{r,i}^{E}=\frac{\varepsilon_0}{2}\int\int\int|\mathbf{E}_{r,i}(\mathbf{r},t)|^2\,d\mathbf{r}=\frac{\varepsilon_0}{8\pi^2}\int_{-\infty}^{+\infty}S_{r,i}(\omega)d\omega. \tag{3.4}$$

Since all the field components are analytic in time at any position **r**, the real and the imaginary solutions are related by a Hilbert transform in time, which leads to

$$S_r(\omega)=S_i(\omega). \tag{3.5}$$

Thus, we have $U_r^E=U_i^E$ and a similar equality for the magnetic energy. Therefore, the real and the imaginary pulse have the same amount of electromagnetic energy. Substituting Eq. (2.4) into Eq. (3.1), the total energy of the exact solution is obtained as

$$U_r=U_i=\frac{3f_0^2\pi^2\mu_0}{16q_2q_1^4}\left\{1+\frac{1}{3}\left(\frac{q_1}{q_2}\right)+\frac{1}{3}\left(\frac{q_1}{q_2}\right)^2+\left(\frac{q_1}{q_2}\right)^3\right\}. \tag{3.6}$$

In the following section, we analyze the evolution of the temporal pulse profile, the spatial distribution of the fields, the amplitude spectra, and other features that are amenable to experimental verification.

IV. PHYSICAL PROPERTIES

A. Paraxial limit ($q_1 \ll q_2$)

The exact solutions given by Eqs. (2.10)–(2.14) simplify considerably in the paraxial or ''weakly focused'' limit where the wavelength q_1 is much smaller than the Rayleigh range q_2. Since this is the limit in which most terahertz systems operate, we provide in this section the appropriate limiting forms of the exact solutions. These approximate solutions are exact solutions of the time-dependent paraxial wave equation and can also be obtained by inverse Fourier transform of the monochromatic fundamental Gaussian beam solution multiplied by the spectrum $\omega^2\exp(-\omega q_1/c)$.

From the radial dependence of the solution it can be seen that the fields have a limited transverse spatial extent. In fact, for $z=ct=0$, the value of E_y at $\rho=\sqrt{q_1q_2}$ is only $\frac{1}{8}$ of its peak value at $\rho=0$. All the other components also drop off at least as rapidly as ρ^{-4}. We thus somewhat arbitrarily define the transverse extent of the beam as $\rho^2\sim q_1q_2$. Outside this range the energy density in the solutions is negligible. The longitudinal extent of these essentially single-cycle pulse solutions is likewise limited by the wavelength to $c\tau_p\sim\pi q_1$, where τ_p is the temporal pulse width. Since the variable $\tau=z-ct$ measures the local distance from the pulse center, the amplitude of the fields is negligible when $|\tau|>c\tau_p$. Thus, wherever the fields have significant amplitude the term $(q_1+i\tau)$ in the solutions can be neglected compared to $(q_2-i\sigma)$ in the limit $q_1\ll q_2$. Furthermore, since the fields are significant only for $\rho^2<q_1q_2$, the term $2\rho^2\cos(2\varphi)$ in Eq. (2.12) is of order $q_1q_2\ll q_2^2$ and can also be neglected compared to $(q_2-i\sigma)^2$. With these approximations, Eqs. (2.10) and (2.12) reduce to

$$E_y(\mathbf{r},t)\approx-\sqrt{\frac{\mu_0}{\varepsilon_0}}H_x(\mathbf{r},t)\approx\frac{-2f_0\mu_0c(q_2-i\sigma)^2}{\{\rho^2+(q_1+i\tau)(q_2-i\sigma)\}^3}. \tag{4.1.1}$$

The relation between $E_y(\mathbf{r},t)$ and $H_x(\mathbf{r},t)$ can also be demonstrated with the use of Maxwell's equation:

$$\boldsymbol{\nabla}\times\mathbf{E}(\mathbf{r},t)=-\mu_0\frac{\delta\mathbf{H}(\mathbf{r},t)}{\partial t}. \tag{4.1.2}$$

Taking Fourier transforms with respect to both time and space yields

$$\hat{\mathbf{k}}\times\tilde{\mathbf{E}}(\omega,\mathbf{k})=\sqrt{\frac{\mu_0}{\varepsilon_0}}\,\tilde{\mathbf{H}}(\omega,\mathbf{k}), \tag{4.1.3}$$

where $\hat{\mathbf{k}}$ is a unit vector in the direction of the wave vector, and is given by

$$\hat{\mathbf{k}}=\hat{\mathbf{x}}\sin\theta\cos\varphi+\hat{\mathbf{y}}\sin\theta\sin\varphi+\hat{\mathbf{z}}\cos\theta. \tag{4.1.4}$$

Substituting Eq. (4.1.4) into (4.1.3) gives

$$\sqrt{\frac{\mu_0}{\varepsilon_0}}\tilde{H}_x(\omega,\mathbf{k})=\sin\theta\sin\varphi\,\tilde{E}_z(\omega,\mathbf{k})-\cos\theta\tilde{E}_y(\omega,\mathbf{k}). \tag{4.1.5}$$

Since $\tilde{E}_z\ll\tilde{E}_y$ [see Eq. (4.1.8)], and $\cos\theta\approx1$ for a weakly diffracting beam, Eq. (4.1.5) reduces to

$$\tilde{E}_y(\omega,\mathbf{k})\approx-\sqrt{\frac{\mu_0}{\varepsilon_0}}\tilde{H}_x(\omega,\mathbf{k}). \tag{4.1.6}$$

An inverse Fourier transform of above equation yields

$$E_y(\mathbf{r},t)\approx-\sqrt{\frac{\mu_0}{\varepsilon_0}}H_x(\mathbf{r},t). \tag{4.1.7}$$

In this weak focusing limit the dominant components of the electromagnetic field turn out to be E_y and H_x. Again replacing ρ^2 by q_1q_2 in Eqs. (2.10)–(2.14), it is easy to see that for $q_1\ll q_2$, the other field components are smaller than E_y and H_x in the ratios

$$\frac{E_z}{E_y}\sim O\left(\sqrt{\frac{q_1}{q_2}}\right),\quad\frac{H_y}{H_x}\sim O\left(\frac{q_1}{q_2}\right),\quad\frac{H_z}{H_x}\sim O\left(\sqrt{\frac{q_1}{q_2}}\right). \tag{4.1.8}$$

Figure 1 shows the spatiotemporal profiles of the five electric and magnetic field components of the real solution at $z=0$. Note that the magnitudes of E_y and H_x greatly exceed that of the other components. Thus, in the weak focusing limit the field is quasi-TEM (transverse electric and magnetic) and quasiaxisymmetric. It has a maximum on axis ($\rho=0$), drops off as ρ^{-4}, has a longitudinal extent ($\sim\pi q_1$) much smaller than its transverse extent ($\sim\sqrt{q_1q_2}$), and thus resembles a pancake. These ''focused pancake'' solutions result from the *x*-directed Hertz potential used in this work as opposed to the *z*-directed potential that led to toroidal ''focused doughnut'' solutions in Ref. [4]. Figure 2(a) shows the energy density at $z=0$ of the real solution

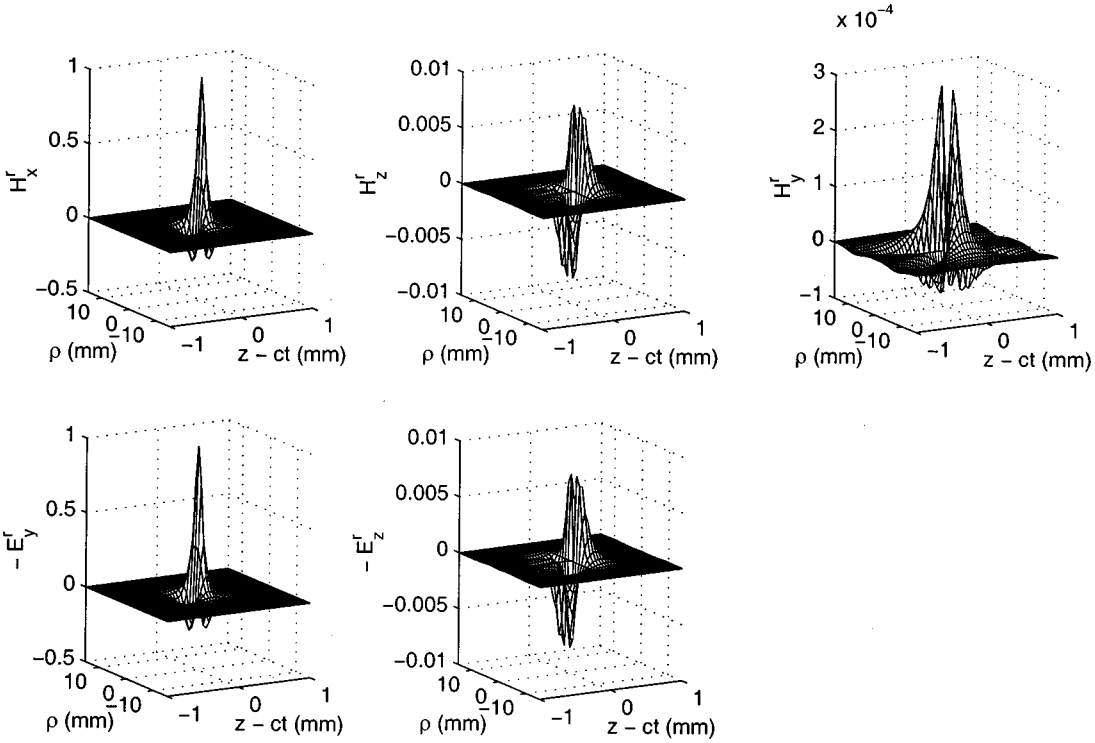

FIG. 1. The five electromagnetic field components corresponding to the real solution $\mathbf{E}^r(\mathbf{r},t)$ and $\mathbf{H}^r(\mathbf{r},t)$. Take $\varphi=\pi/4$ in the field Eqs. (2.10)–(2.14). The electric fields are normalized by the peak value of E_y^r, while the magnetic fields are normalized by the peak value of H_x^r. Note that E_y^r and H_x^r are the dominant field components. In this and subsequent plots we have chosen $q_1=0.1$ mm and $q_2=100$ mm, parameters appropriate for terahertz pulses.

$$U_r(\mathbf{r},t)=\tfrac{1}{2}\{\varepsilon_0|\mathbf{E}_r|^2+\mu_0|\mathbf{H}_r|^2\}$$

based on the exact expressions in Eqs. (2.10)–(2.14). The energy density based on the approximate solution of Eq. (4.1.1) is shown in Fig. 2(b). The two plots are indistinguishable and show the flat, ''pancake'' nature of the solutions.

In the limit $q_1 \ll q_2$, the solutions (2.10)–(2.14) describe the spatiotemporal evolution of focused electromagnetic pulses that have a near-Gaussian transverse beam profile and attain a minimum spot size in the plane $z=0$, which we will call the focal plane. To visualize these pulses and relate them to terahertz experiments, we set the parameters $q_1=0.1$ mm and $q_2=100$ mm, and plot in Fig. 3 the on-axis ($\rho=0$) temporal shapes of the real (E_y^r) and imaginary (E_y^i) parts of E_y at $z=0$. In this plane E_y^r is symmetric in time and passes through zero twice while E_y^i is antisymmetric and goes through zero three times. These fields therefore represent pulses that are essentially single cycle in nature.

We define the pulse width, somewhat arbitrarily as the separation between the two side nulls of the imaginary pulse. To estimate this pulse width we use the fact that, for a single-cycle pulse, the spatial extent in the propagation direction $c\tau_p$ is of order $\pi q_1 \ll q_2$. Hence at $\mathbf{r}=0$, the factor $(q_1 - ict)$ is much smaller in magnitude than $(q_2 - ict)$. Writing these factors in terms of magnitude and phase, we find that $E_y^i(0,t)$ is proportional to $\sin(3\phi_1)$, where $\phi_1=\tan^{-1}(ct/q_1)$ and we use the approximation $ct \ll q_2$ wherever the field has significant amplitude. The separation between the two side nulls of $E_y^i(0,t)$ is thus

$$\tau_p(\mathbf{r}=0)=2\sqrt{3}\,\frac{q_1}{c}. \tag{4.1.9}$$

For $q_1=0.1$ mm this yields a pulse width of 1.15 ps. While this expression has been derived for the imaginary pulse, Fig. 3 shows that the real solution has roughly the same pulse width.

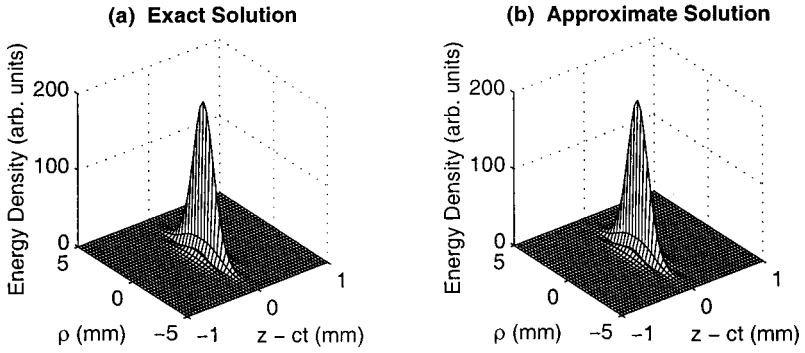

FIG. 2. Energy density of the real solution at $z=0$. (a) From the exact expressions of Eqs. (2.10)–(2.14). The values are calculated on the plane that contains propagation axis z and bisects the x-y plane, i.e., $\varphi=\pi/4$. (b) From the approximate expression, Eq. (4.1.1).

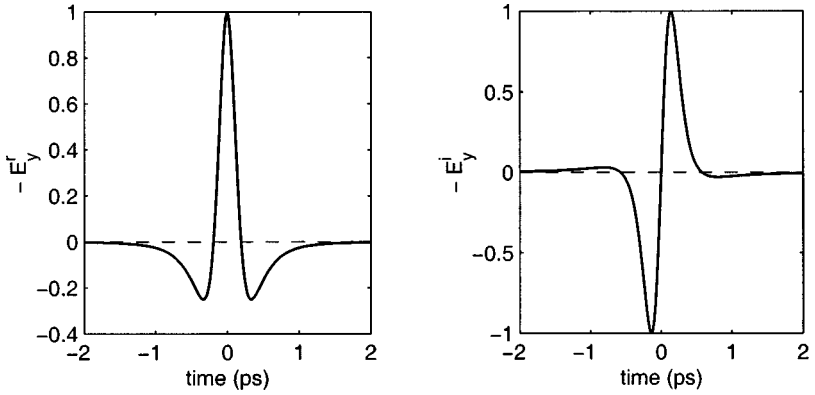

FIG. 3. On-axis pulse temporal shapes at $z=0$ for the real and the imaginary solutions. The fields are normalized by their peak values.

B. Spatiotemporal evolution of pulses

Figure 4 shows the spatiotemporal evolution of the real and imaginary pulse solutions from a distant plane ($z=-30$ cm) before the focus, through the focus and then to a plane in the far field ($z=30$ cm). The variable $z-ct$ represents the local distance measured from the pulse center and ρ is the radial coordinate. One clearly observes the curved phase fronts of the pulse as it converges to a minimum spot size at the focus and then diverges again. More significantly we observe a polarity reversal and substantial temporal reshaping as the pulse evolves through the focus. A similar polarity reversal for half-cycle pulses has been noted by You and Bucksbaum [7]. The temporal reshaping that accompanies free space propagation can be more easily analyzed by following the temporal profile of the pulse along the z axis ($\rho=0$). Figure 5 shows the axial temporal profiles of the real and the imaginary solutions at several propagation distances. It is seen that the symmetric real solution at $z=0$ evolves in the far field into an inverted version of the antisymmetric imaginary pulse at $z=0$. Simultaneously, the antisymmetric imaginary solution at $z=0$ evolves in the far field into the symmetric real solution. The transformation of a pulse temporal profile from symmetric to antisymmetric as it propagates from the focus has been observed in terahertz experiments by Budiarto *et al.* [8]. It is important to note the striking difference in the way the real and imaginary pulses transform as they propagate through the focus from a point $-z$ to a point z. It is evident from Fig. 5 that the real solution

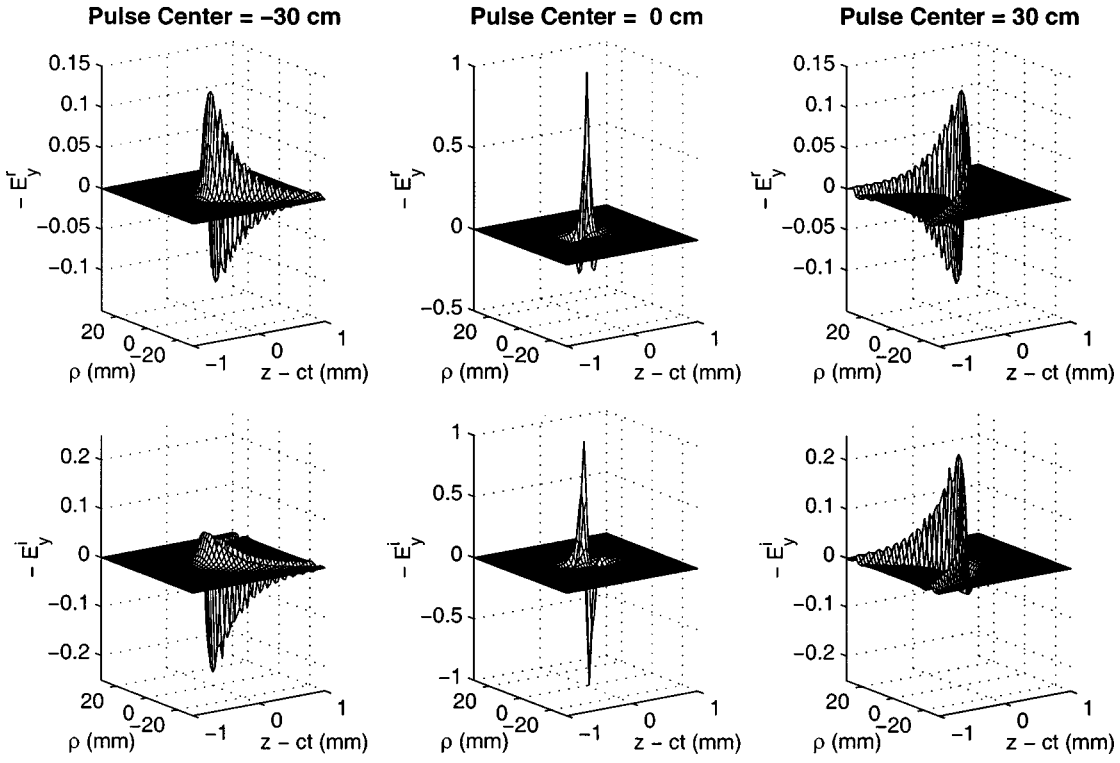

FIG. 4. Spatiotemporal evolution of the real (top) and the imaginary (bottom) pulses from the plane ($z=-30$ cm), passing through the focus, to the plane ($z=30$ cm). The variable $z-ct$ represents the local distance measured from the pulse center and ρ is the radial coordinate. One clearly observes the curved phase fronts, the polarity reversal and the temporal reshaping as the pulse evolves through the focus. The plots are normalized by the peak value at the focus.

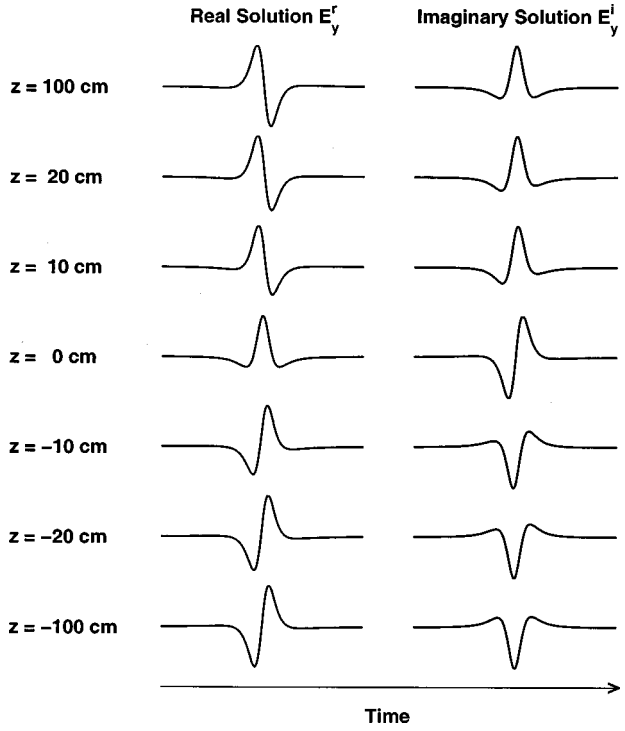

FIG. 5. Temporal profiles on axis at several propagation distances for the real and the imaginary solutions. The two solutions have the following symmetries: $E^r(-z,t)=E^r(z,-t)$ and $E^i(-z,t)=-E^i(z,-t)$. Thus in passing through the focus the real solution undergoes a time reversal while the imaginary solution undergoes both time reversal and polarity reversal.

E^r undergoes a time reversal while the imaginary solution undergoes both a time reversal and a polarity reversal.

C. Effect of Gouy phase shift

The change in pulse waveform under focusing can be explained by the difference of phase and envelope velocity in the focal region and is related to the Gouy phase shift of focused beams.

In the limit $q_1 \ll q_2$, σ can be replaced by $2z$ in Eq. (4.1.1), and the complex field can be rewritten as

$$E_y(\mathbf{r},t)\approx \frac{-2f_0\mu_0 c}{(q_2-i2z)} \times \frac{1}{\left\{ q_1+\frac{q_2\rho^2}{4z^2+q_2^2}+i\left(z-ct+\frac{2z\rho^2}{4z^2+q_2^2}\right)\right\}^3}. \tag{4.3.1}$$

Note that the replacement of σ by $2z$ does not affect the analyticity of the field. The poles of Eq. (4.3.1) are still in the lower half-plane for any spatial point, hence Eq. (4.3.1) is also an analytic function of time at any point in space. After much algebra we obtain a particularly useful form for the field:

$$E_y(\mathbf{r},T)=\frac{A(T)}{\sqrt{z_0^2+z^2}\left\{1+\frac{\rho^2}{2w^2(z)}\right\}^3}\exp\{i[\alpha(T)+\phi(z)]\}, \tag{4.3.2}$$

where T is a radially scaled local time (SLT), given by

$$T=\frac{c\left\{t-\frac{z+\rho^2/2R(z)}{c}\right\}}{q_1\left\{1+\frac{\rho^2}{2w^2(z)}\right\}}. \tag{4.3.3}$$

Here

$$R(z)=z\left\{1+\left(\frac{z_0}{z}\right)^2\right\},$$

$$w^2(z)=w_e^2\left\{1+\left(\frac{z}{z_0}\right)^2\right\}, \tag{4.3.4}$$

$$w_e^2=\frac{q_1q_2}{2},\quad z_0=\frac{q_2}{2},$$

and

$$\phi(z)=\tan^{-1}\left(\frac{z}{z_0}\right),\quad A(T)=\frac{-f_0\mu_0 c}{q_1^3(T^2+1)^{3/2}},$$

$$\alpha(T)=3\tan^{-1}(T). \tag{4.3.5}$$

The quantity $R(z)$ represents the radius of curvature of the pulse wave front while $w(z)$ measures the transverse extent of the beam. Although the transverse beam profile is clearly non-Gaussian we will show later that the beam energy diffracts in the same manner as a monochromatic Gaussian beam with an effective beam waist $w_e=\sqrt{q_1q_2/2}$ and Rayleigh range $z_0=q_2/2$. The term $\{z+\rho^2/2R(z)\}/c$ in T is the radially-dependent delay suffered by the pulse during propagation. The edges of the pulse are delayed more than the center and this results in a curved wave front. The quantity $\{1+\rho^2/2w^2(z)\}$ in T scales the pulse width and hence the pulse width is different at different radial positions. However, along the hyperbolic trajectories $\rho^2/w^2(z)=\text{const}$, the pulse width is invariant. The quantity $\phi(z)=\tan^{-1}(z/z_0)$ is the Gouy phase shift that any finite beam encounters upon passage through a focus.

The real and the imaginary parts of Eq. (4.3.2) represent the spatiotemporal evolution of the physical pulse solutions of Maxwell's equations in the paraxial limit and are given by

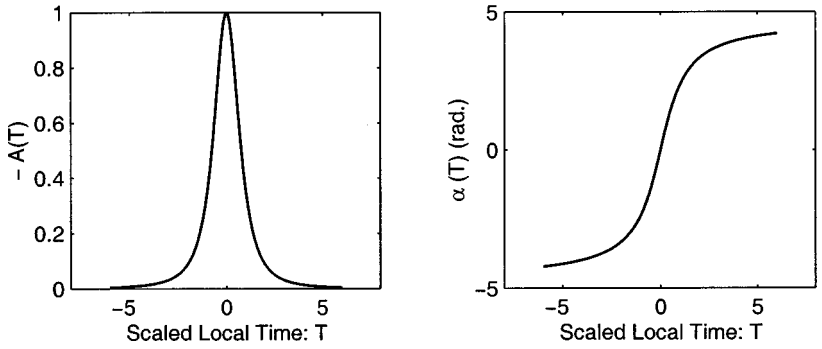

FIG. 6. Amplitude function and temporal phase function. Note the horizontal axis is dimensionless local time.

$$E_y^r(\mathbf{r},T)=\frac{A(T)}{\sqrt{z_0^2+z^2}\left\{1+\dfrac{\rho^2}{2w^2(z)}\right\}^3}\cos[\alpha(T)+\phi(z)],$$

$$E_y^i(\mathbf{r},T)=\frac{A(T)}{\sqrt{z_0^2+z^2}\left\{1+\dfrac{\rho^2}{2w^2(z)}\right\}^3}\sin[\alpha(T)+\phi(z)]. \tag{4.3.6}$$

The temporal envelope function $A(T)$ and the phase function $\alpha(T)$ are invariant upon propagation (except for the scaling in time for the points off axis) since they depend only on the scaled local time T. Figure 6 shows the form of these functions. Any variation of the spatiotemporal profiles of the pulse $E_y^{r,i}(\mathbf{r},T)$ during propagation is completely determined by the Gouy phase shift $\phi(z)$, which modulates the initial phase of the temporal functions of the fields. The factor $(z_0^2+z^2)^{-1/2}[1+\rho^2/2w^2]^{-3}$ accounts for energy conservation due to the propagation and the scaling. In propagation from the focus to the far field $\phi(z)$ goes from zero to $\pi/2$, thus effecting the transformation $E_y^r\rightarrow -E_y^i$ and $E_y^i\rightarrow E_y^r$. This transformation is also obtainable from the Hilbert transform relationship between the real and imaginary parts of the complex field. The $\pm\pi/2$-phase shift in each frequency component in propagating from $z=0$ to $z\rightarrow\pm\infty$ results in a Hilbert transform in time between the near field and the far field. The Gouy shift is thus responsible for the pulse reshaping, time reversal, and polarity reversal that occurs when these pulses pass through the focus.

To emphasize the validity of the approximations leading to Eq. (4.3.6), Fig. 7 shows the pulse profiles on axis at $z=10$ cm as calculated from the exact formula Eq. (2.10) and from the approximate formula Eq. (4.3.6).

The field solutions obey the following space-time symmetries [9]:

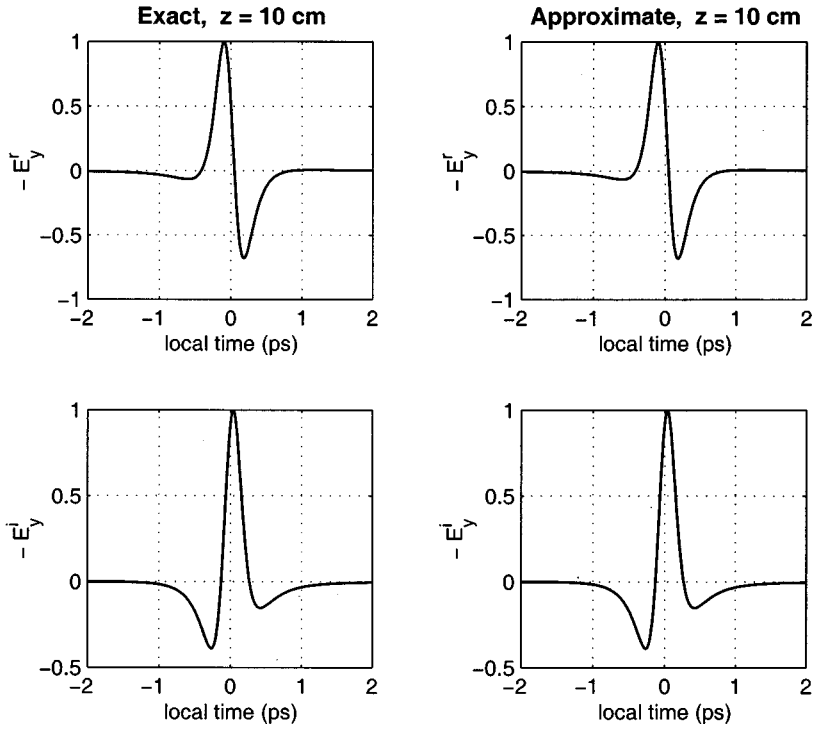

FIG. 7. Temporal profiles of the pulses at $z=10$ cm for the real and imaginary solutions. The plots on the left are from the exact solution Eq. (2.10), while the plots on the right are from the approximate solution Eq. (4.3.6). The fields are normalized by their peak values.

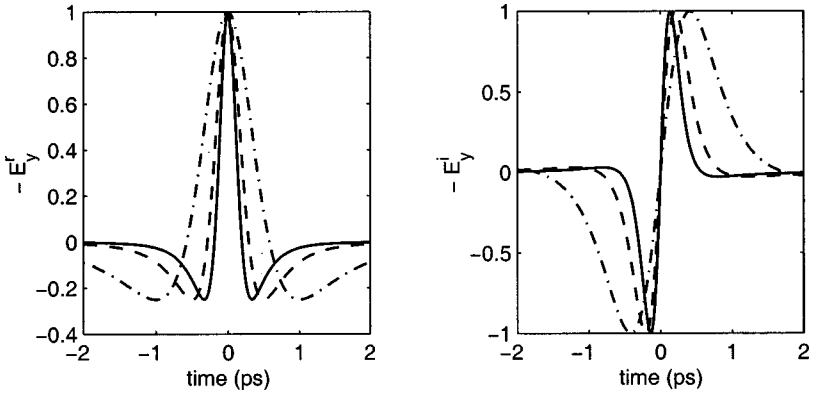

FIG. 8. Dependence of pulse shapes on radial position at $\rho=0$ (solid line), $\rho=w_e$ (dashed line), and $\rho=2w_e$ (dot-dashed line), where w_e is the effective beam waist. The fields are normalized by their peak values.

$$E_y^r(-z,-T)=E_y^r(z,T); \quad E_y^i(-z,-T)=-E_y^i(z,T). \tag{4.3.7}$$

The real pulse is symmetric under the reflection of both space and time, while the imaginary pulse is antisymmetric. This explains why in passing through the focus the imaginary pulse is both time reversed and inverted while the real pulse is only time reversed.

A key feature of these pulse solutions is that they are not separable into a product of a function that depends only on time and one that depends only on space. One consequence of this nonseparability is that the pulse width is generally dependent on radial position and propagation distance. From Eqs. (4.1.9) and (4.3.3), it can be shown that the pulse width at any position $\mathbf{r}$ is given by

$$\tau_p(\mathbf{r})=2\sqrt{3}\,\frac{q_1}{c}\left\{1+\frac{\rho^2}{2w^2(z)}\right\}. \tag{4.3.8}$$

The minimum pulse width occurs on axis ($\rho=0$) and is invariant with propagation distance. Off axis the pulse width is longer by a factor of $\{1+\rho^2/2w^2(z)\}$, and it decreases with propagation distance for fixed ρ.

As shown in Sec. IV E, in the frequency domain these pulses consist of an ensemble of Gaussian beams of different frequencies, all of which have the same Rayleigh range $z_0=q_2/2$. For a Gaussian beam of wavelength λ and beam waist w_0, the Rayleigh range is given by $z_0=\pi w_0^2/\lambda$. In order that z_0 remains fixed at all wavelengths the beam waists must scale as $w_0\propto\sqrt{\lambda}$. Thus, in any transverse plane the higher frequency components of the pulse are closely confined to the axis while the lower frequency components are more spread out. It is this radial dispersion of beam waists that leads to the radial dependence of the pulse widths. Figure 8 shows the temporal profiles of the real and imaginary pulse solutions at $z=0$ for $\rho=0$, $\rho=w_e$, and $\rho=2w_e$. The radial dependence of the pulse widths in any fixed z plane is also true in the far field.

We note that Kaplan has also discussed a radial dependence of pulse widths due to the different diffraction angle for frequency components with the same initial waist (Ref. [9]) while Wang *et al.* (Ref. [10]) have analyzed a situation similar to ours where the beam waists scale as $\sqrt{\lambda}$. In recent experiments, Budiarto *et al.* [8], have observed dramatic increases in pulse width as a function of radial distance from the axis at the focus of terahertz beams. The pulse widths appear to increase linearly with radial distance as might be expected for a pulse the frequency components of which have the same geometrical f number. This is closer to the situation analyzed by Kaplan [9].

The results of Eq. (4.3.6) show that a pure phase change $\phi(z)$ can lead to dramatic reshaping of a single-cycle terahertz pulse. In fact, experiments have revealed how the phase shift on total internal reflection distorts the temporal profile of an incident pulse (Ref. [11]). We suggest that Eq. (4.3.6) can be used, along with a measurement of initial and final pulse shapes, to extract the phase shift responsible for pulse shaping.

D. Hilbert transform relationship between near and far field

As pointed out earlier, since the complex field solution $E_y(\mathbf{r},t)$ is an analytic function of time at any point $\mathbf{r}$, its real and imaginary parts are Hilbert transforms of each other with respect to the global time variable t. We now show that the temporal profiles in the far field are Hilbert transforms of the temporal profiles in the focal plane ($z=0$). In other words, propagation from the focus to the far field corresponds to a Hilbert transform operation performed with respect to the local time.

Because of the transverse spreading of the pulse due to diffraction, it is convenient to compare temporal profiles in the near field ($z=0$) and far field ($z\to\infty$) for points that have the same radial coordinate relative to the z-dependent beam radius $w(z)$. Such points are defined by $\rho^2/2w^2(z)=\text{const}\equiv\mu$, which specifies the hyperbolic trajectories

$$\rho^2-2\mu z^2\left(\frac{w_e}{z_0}\right)^2=2\mu w_e^2. \tag{4.4.1}$$

Along these trajectories the scaled local time becomes

$$T_\mu=\frac{c\left\{t-\dfrac{z}{c}\left[1+\mu\dfrac{q_1}{z_0}\right]\right\}}{q_1(1+\mu)}. \tag{4.4.2}$$

At $z=0$, the real and the imaginary parts of the complex field are given by the Hilbert transform pair

$$E_y^r(z=0,T_\mu)=\frac{A(T_\mu)\cos[\alpha(T_\mu)]}{z_0(1+\mu)^3}=\mathcal{H}\{E_y^i(z=0,T_\mu)\}, \tag{4.4.3}$$

$$\begin{aligned}E_y^i(z=0,T_\mu)&=\frac{A(T_\mu)\sin[\alpha(T_\mu)]}{z_0(1+\mu)^3}\\&=\mathcal{H}^{-1}\{E_y^r(z=0,T_\mu)\}\\&=-\mathcal{H}\{E_y^r(z=0,T_\mu)\}.\end{aligned}$$

In the far field, as $z\to+\infty$, $\phi(z)\to\pi/2$, hence the fields become

$$\begin{aligned}E_y^r(z\to+\infty,T_\mu)&=-\frac{A(T_\mu)\sin[\alpha(T_\mu)]}{z_0\sqrt{1+(z/z_0)^2}(1+\mu)^3}\\&=\frac{1}{\sqrt{1+(z/z_0)^2}}\mathcal{H}\{E_y^r(z=0,T_\mu)\},\end{aligned} \tag{4.4.4}$$

$$\begin{aligned}E_y^i(z\to+\infty,T_\mu)&=\frac{A(T_\mu)\cos[\alpha(T_\mu)]}{z_0\sqrt{1+(z/z_0)^2}(1+\mu)^3}\\&=\frac{1}{\sqrt{1+(z/z_0)^2}}\mathcal{H}\{E_y^i(z=0,T_\mu)\}.\end{aligned}$$

Equation (4.4.4) show that for points in the near field and the far field that have the same relative transverse coordinate $\rho/w(z)$, the temporal profiles are related by a Hilbert transform.

More generally, for any two points ($z_1=0$, $\rho=\rho_1$) and ($z_2\to+\infty$, $\rho=\rho_2$) that do not necessarily lie on the hyperbolic trajectories described above (the pulse width is different), a scaled Hilbert transform relation exists between the temporal profiles at the two points:

$$E_y^r(z_2,\rho_2,\zeta)=\frac{s^3}{d\pi}\mathrm{P}\int_{-\infty}^{+\infty}\frac{E_y^r(0,\rho_1,t')}{s\zeta-t'}dt', \tag{4.4.5}$$

$$E_y^i(z_2,\rho_2,\zeta)=-\frac{s^3}{d\pi}\mathrm{P}\int_{-\infty}^{+\infty}\frac{E_y^i(0,\rho_1,t')}{s\zeta-t'}dt'.$$

Here

$$\zeta\equiv t-\frac{z_2+\dfrac{\rho_2^2}{2R(z_2)}}{c}, \tag{4.4.6}$$

and the scaling parameter s is given by

$$s=\frac{1+\dfrac{\rho_1^2}{q_1q_2}}{1+\dfrac{\rho_2^2}{2w^2(z_2)}}, \tag{4.4.7}$$

and $d=\sqrt{1+[z_2/z_0]^2}$. The factor s^3/d in front of Eq. (4.4.5) accounts for energy conservation due to the propagation and the scaling.

It is often stated that the far field temporal distribution is a time derivative of the near field temporal distribution. An examination of the Kirchhoff diffraction law for nonmonochromatic fields shows that this derivative relationship is strictly true if the initial distribution is separable into a spatial function multiplied by a temporal function. If the initial distribution is nonseparable, different radial positions will have different temporal profiles. In that case the time derivative is with respect to the temporal profile of the total field integrated over the transverse plane. In the time domain the Kirchhoff diffraction law is given by [12]:

$$E(P_0,t)=\int\int_\Sigma\frac{\cos(n,r)}{2\pi c r_{10}}\frac{d}{dt}E\left(P_1,t-\frac{r_{01}}{c}\right)ds.$$

Figure 9(a) shows the results of applying the Hilbert transform relation and an application of the Kirchhoff diffraction law to the initial field distribution. As expected, the two approaches agree. Figure 9(b) shows the evolution of the spatiotemporal field profile obtained by using the Kirchhoff diffraction law. This should be compared with Fig. 4, which was generated from the exact solutions given by Eqs. (2.10)–(2.14).

E. Fourier transform of the field

We now turn to a frequency domain description of the exact pulse solutions obtained in Sec. II.

From Eq. (2.8), we have

$$E_y(\mathbf{r},t)=-\mu_0\frac{\partial}{\partial t}\left(\frac{\partial f}{\partial z}\right). \tag{4.5.1}$$

With the definition of the Fourier transform given by Eq. (2.17), and using the fact that the field vanishes as $t\to\pm\infty$, a Fourier transform of Eq. (4.5.1) gives

$$\tilde{E}_y(\mathbf{r},\omega)=-i\mu_0\omega\int_{-\infty}^{+\infty}\frac{\partial f(\mathbf{r},t)}{\partial z}\exp(-i\omega t)dt. \tag{4.5.2}$$

The Fourier transform can be evaluated by means of a contour integral around a path that encloses two double poles in the lower half-plane. For $\omega>0$, the integration yields

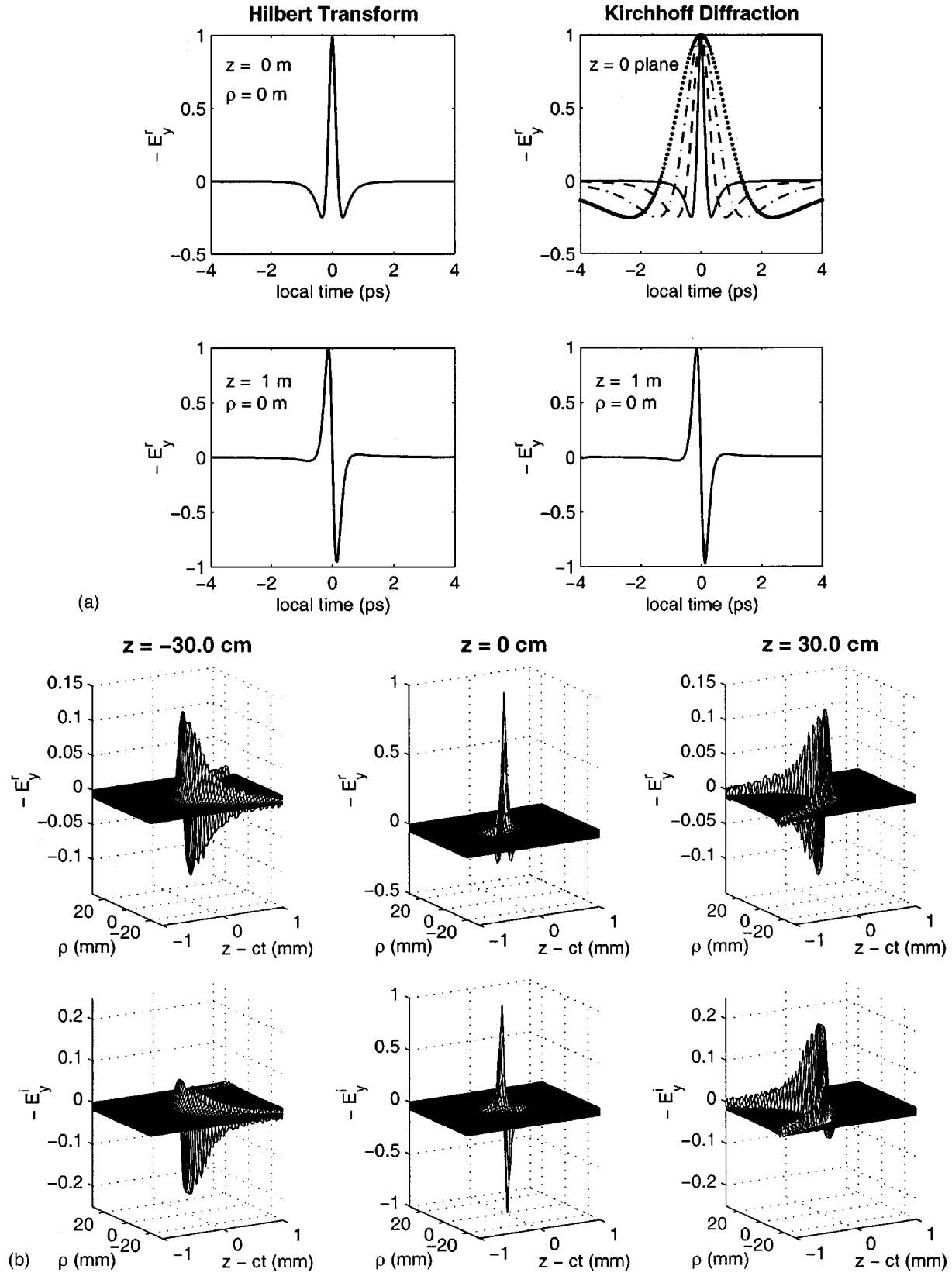

FIG. 9. (a) The near-field and the far-field temporal wave forms of the real solution. The plot on the lower left is a Hilbert transform of the plot on the upper left. The plot on the lower right is obtained from the Kirchhoff diffraction integral. It is a time derivative of a field integrated over the diffracting screen ($z=0$); i.e., a summation of the temporal profiles in the upper right plot where only four temporal profiles are shown. Note the temporal functions are different for different ρ's on the $z=0$ plane. The fields are normalized by their peak values. (b) Simulations of the spatiotemporal evolutions of the real (top) and the imaginary (bottom) solutions using the time-domain Kirchhoff diffraction integral for a comparison with Fig. 4 which is plotted from the analytical solutions. The plots are normalized by the peak value at the focus.

$$\tilde{E}_y(\mathbf{r},\omega)=\frac{\pi f_0\mu_0\omega}{c}\frac{\exp\left[-\frac{k}{2}(q_1+q_2)\right]\left\{\left(\frac{1}{\beta}-ik\right)\exp(ik\beta)-\left(\frac{1}{\beta}+ik\right)\exp(-ik\beta)\right\}}{\left(z+i\frac{q_2-q_1}{2}\right)\left\{1+\frac{\rho^2}{\left(z+i\frac{q_2-q_1}{2}\right)^2}\right\}},\tag{4.5.3}$$

where

$$\beta\equiv\left\{\rho^2+\left(z+i\frac{q_2-q_1}{2}\right)^2\right\}^{1/2}.\tag{4.5.4}$$

For $\omega\leqslant 0$ the integral is zero. Since the time-domain complex field is given by

$$E_y(\mathbf{r},t)=E_y^r(\mathbf{r},t)+iE_y^i(\mathbf{r},t),\tag{4.5.5}$$

the spectrum of the real and imaginary parts can be computed from

$$\begin{aligned}\tilde{E}_y^r(\mathbf{r},\omega)&=\tfrac{1}{2}\{\tilde{E}_y(\mathbf{r},\omega)+\tilde{E}_y^*(\mathbf{r},-\omega)\},\\ \tilde{E}_y^i(\mathbf{r},\omega)&=\frac{1}{2i}\{\tilde{E}_y(\mathbf{r},\omega)-\tilde{E}_y^*(\mathbf{r},-\omega)\}.\end{aligned}\tag{4.5.6}$$

With the property $\tilde{E}_y(\mathbf{r},\omega)=0$ for $\omega\leqslant 0$, it can be shown that the Fourier transforms of the real and imaginary solutions are related by Eq. (2.18) which is the Hilbert transform relationship demonstrated in the frequency domain.

From Eq. (4.5.3) we see that the field is composed of two counter-propagating waves. With the definition of the Fourier transform as given by Eq. (2.17), it is recognized that the term in $e^{-ik\beta}$ represents a forward propagating field, while the term in $e^{ik\beta}$ represents the backward field component.

Equation (4.5.3) is exact. In the weak focusing limit $q_1 \ll q_2$, Eq. (4.5.3) can be greatly simplified. Since $\rho^2\sim q_1q_2 \ll q_2^2$ wherever the field has significant amplitude, the ρ^2 term in the denominator can be neglected. Keeping terms of first order in ρ^2 in the exponents, it is found that the backward field component ($\sim e^{-kq_2}$) is much smaller than the forward field ($\sim e^{-kq_1}$), and hence can be neglected. In the forward component, the quantity $1/\beta$ is of order i/q_2, which in turn is much smaller than ik. Hence, replacing $(1/\beta)+ik$ by ik, Eq. (4.5.3) is reduced to

$$\tilde{E}_y(\mathbf{r},\omega)=\begin{cases}-i\dfrac{2\pi f_0\mu_0\omega^2}{c^2}\dfrac{1}{2z+iq_2}\exp\{-ik(z-\alpha_r)-k\alpha_i\}, & \omega>0,\\ 0, & \omega\leqslant 0,\end{cases}\tag{4.5.7}$$

where

$$\alpha_r=-\frac{2z\rho^2}{4z^2+q_2^2},\quad \alpha_i=q_1+\frac{\rho^2q_2}{4z^2+q_2^2}.\tag{4.5.8}$$

Substituting Eq. (4.5.7) into Eq. (4.5.6), we obtain the spectra of the real and imaginary pulses as

$$\tilde{E}_y^r(\mathbf{r},\omega)=-i\frac{\pi f_0\mu_0\omega|\omega|}{c^2}\frac{\exp\{-ik(z-\alpha_r)\}}{2z+i\frac{\omega}{|\omega|}q_2}\times\exp\left\{-\frac{|\omega|}{c}\alpha_i\right\},\qquad -\infty<\omega<+\infty,$$

$$\tilde{E}_y^i(\mathbf{r},\omega)=-\frac{\pi f_0\mu_0\omega^2}{c^2}\frac{\exp\{-ik(z-\alpha_r)\}}{2z+i\frac{\omega}{|\omega|}q_2}\times\exp\left\{-\frac{|\omega|}{c}\alpha_i\right\},\qquad -\infty<\omega<+\infty.\tag{4.5.9}$$

These results are also obtainable from the direct Fourier transform of the approximate solutions.

F. Pulse diffraction

The ultrashort pulse width of a single-cycle pulse results in an extremely broad bandwidth. Each frequency component of the pulse propagates independently. The diffraction character of the entire pulse, such as its spatial profile in any transverse plane, is determined by the diffraction nature of each frequency component of the pulse. The diffraction of the pulse is analyzed in two ways in this section: (i) the

diffraction of each frequency component and (ii) the diffraction of the entire pulse treated as a single entity. We find that in the weak focusing limit each frequency component diffracts like a conventional Gaussian beam with a different beam waist but the same Rayleigh range for all the frequencies. The entire pulse is not Gaussian in space or time. However, the rate of spread of the transverse energy distribution is similar to that of a monochromatic Gaussian beam with an effective wavelength of πq_1.

Equation (4.5.9) can be rewritten in the form of a conventional Gaussian beam weighted by a frequency-dependent factor. Substituting Eq. (4.5.8) into Eq. (4.5.9) we find

$$\tilde{E}_y^r(\mathbf{r},\omega)=\frac{-\pi f_0\mu_0}{\sqrt{q_2}w}\left(\frac{|\omega|}{c}\right)^{3/2}\exp\left\{-\frac{|\omega|}{c}q_1\right\}\times\exp\left\{-ikz+i\frac{\omega}{|\omega|}\phi-ik\frac{\rho^2}{2R}-\frac{\rho^2}{w^2}\right\}, \tag{4.6.1a}$$

$$\tilde{E}_y^i(\mathbf{r},\omega)=i\frac{\omega}{|\omega|}\tilde{E}_y^r(\mathbf{r},\omega), \tag{4.6.1b}$$

where the beam radius $w(z)$, the radius of curvature $R(z)$, the Gouy phase shift $\phi(z)$, the beam waist w_0, and the Rayleigh range z_0, respectively, are given by

$$w^2=w_0^2\left\{1+\left(\frac{z}{z_0}\right)^2\right\}, \tag{4.6.2}$$

$$R=z\left\{1+\left(\frac{z_0}{z}\right)^2\right\}, \tag{4.6.3}$$

$$\phi=\tan^{-1}\left(\frac{z}{z_0}\right), \tag{4.6.4}$$

$$w_0^2=\frac{\lambda q_2}{2\pi}, \tag{4.6.5}$$

$$z_0\equiv\frac{\pi w_0^2}{\lambda}=\frac{q_2}{2}. \tag{4.6.6}$$

The beam waist of each frequency component is proportional to $\sqrt{\lambda}$. The far-field diffraction angle of each frequency component is given by

$$\theta_f=\frac{w(z)}{z}\approx\frac{\lambda}{\pi w_0}=\sqrt{\frac{2\lambda}{\pi q_2}}, \tag{4.6.7}$$

which is also proportional to $\sqrt{\lambda}$. The above equations clearly show that each frequency component in the single-cycle pulse propagates independently as a conventional Gaussian beam weighted by a frequency-dependent factor which is zero at dc and decays exponentially in the high frequency end. The parameter q_2 is seen to play the role of the confocal parameter which is twice the Rayleigh range: the distance from the waist $(z=0)$ to the plane in which the beam area is twice that at the waist. It is important to note that all the frequency components are characterized by the same value of q_2 and hence will all have the same Rayleigh range. From the definition of the beam waist w_0 it is clear that if q_2 is fixed, the longer wavelength components will have a larger spot size at the focus. By tailoring the beam waist, all the frequency components have the same Rayleigh range, which means the rate of the beam spreading and energy decay on the transverse plane is the same for all the frequencies. Thus the spatially resolved spectral profile on axis is invariant on propagation except that the magnitude of the entire spectrum is scaled down by an intensity decay factor. This is shown in Fig. 10 in which the frequency of the peak intensity and the full width at half-maximum (FWHM) bandwidth are independent of propagation distance. This result is confirmed by Eqs. (4.7.2) and (4.7.3) in Sec. IV G. Since all the components have the same Rayleigh range, the transition between near field and far field will occur at the same point for all the frequencies. It is this feature that makes it possible for the pulse to propagate as an entity without dispersing away. This suggests a practical way to create such pulses is with a confocal resonator which ensures that all wavelength components have the same Rayleigh range.

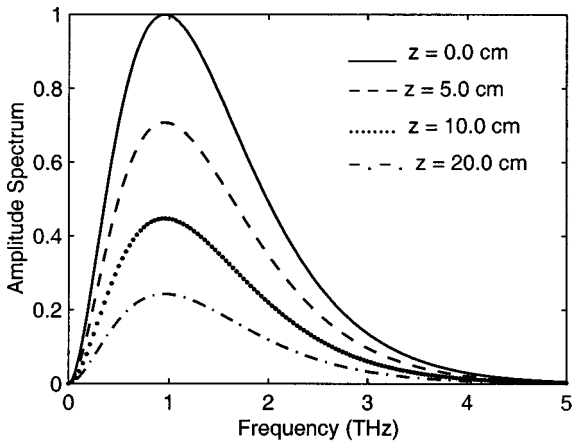

FIG. 10. A plot of amplitude spectra on axis at different propagation distances. The spectra are normalized by the peak value of the spectrum at the focus $(z=0,\rho=0)$. The peak frequencies and FWHM bandwidths are invariant on propagation. The magnitude of each spectrum is simply scaled by a decay factor due to the diffraction.

An alternative approach to pulse diffraction is to consider the distribution of the entire pulse energy on the transverse planes at different propagation distances. The total energy passing through each plane should be conserved during propagation. The beam spread during propagation leads to a continuous decay of the energy density in the x-y plane. The physical quantity which characterizes the energy distribution on the transverse planes is given by

$$\Gamma(\mathbf{r})\equiv\int P_z^r(\mathbf{r},t)dt=\int P_z^i(\mathbf{r},t)dt, \tag{4.6.8}$$

where P_z^r and P_z^i are, respectively, the Poynting vectors of the real and imaginary pulses. Since only the components E_y and H_x are significant, we have

$$P_z^r(\mathbf{r},t)=-E_y^r(\mathbf{r},t)H_x^r(\mathbf{r},t);\quad P_z^i(\mathbf{r},t)=-E_y^i(\mathbf{r},t)H_x^i(\mathbf{r},t). \tag{4.6.9}$$

From Eq. (4.1.1) and the Parseval equation, Eq. (4.6.8) can be expressed as

$$\Gamma(\mathbf{r})=\frac{c\varepsilon_0}{2\pi}\int_{-\infty}^{+\infty}|\tilde{E}_y^r(\mathbf{r},\omega)|^2\,d\omega=\frac{c\varepsilon_0}{2\pi}\int_{-\infty}^{+\infty}|\tilde{E}_y^i(\mathbf{r},\omega)|^2\,d\omega. \tag{4.6.10}$$

The quantity $\Gamma(\mathbf{r})$ has dimensions of energy per area. It describes the distribution of the pulse energy on the transverse planes at different propagation distances. This distribution is the same for the real and the imaginary solutions. Substituting Eq. (4.6.1) into Eq. (4.6.10) we obtain

$$\Gamma(\mathbf{r})=\frac{3\pi f_0^2\mu_0}{4q_1^5}\frac{1}{(4z^2+q_2^2)\left\{1+\dfrac{q_2\rho^2}{q_1(4z^2+q_2^2)}\right\}^5}. \tag{4.6.11}$$

This equation describes the distribution of energy density on any transverse plane z and can be used to describe the diffraction of the entire pulse. To determine the beam size in the radial direction at different translation positions, we consider the ratio

$$\frac{\Gamma(\rho,z)}{\Gamma(0,z)}=\frac{1}{\left\{1+\dfrac{q_2\rho^2}{q_1(4z^2+q_2^2)}\right\}^5}=\frac{1}{\left\{1+\dfrac{\rho^2}{2w^2(z)}\right\}^5}. \tag{4.6.12}$$

where we have defined

$$w^2=w_e^2\left\{1+\left(\frac{z}{z_0}\right)^2\right\}, \tag{4.6.13}$$

with

$$w_e^2\equiv\tfrac{1}{2}q_1q_2,\quad z_0\equiv\tfrac{1}{2}q_2. \tag{4.6.14}$$

When $\rho=w$, the ratio $\Gamma(w,z)/\Gamma(0,z)$ equals $(2/3)^5\approx0.132$. This value is remarkably close to $e^{-2}\approx0.135$. We thus note that the Gaussian beam criterion $\Gamma(w,z)/\Gamma(0,z)=e^{-2}$ leads to a consistent definition of beam radius w for the entire pulse as given in Eq. (4.6.13).

The quantity w^2 in Eq. (4.6.13) is proportional to the beam area of the entire pulse as it propagates through space. It has the same mathematical form as the beam area of a monochromatic Gaussian beam with a waist of $(q_1q_2/2)^{1/2}$ and a Rayleigh range of $q_2/2$. Therefore, w_e and z_0 in Eq. (4.6.14) can be used to define, respectively, the effective beam waist and Rayleigh range of single-cycle pulses. Note that $q_2/2$ is the Rayleigh range of the entire pulse, as well as each frequency component of the pulse. After propagating a distance of Rayleigh length, the beam area of each frequency component, as well as the entire pulse, increases by the same factor; therefore, the spectra on axis are invariant during propagation. This invariance is achieved by making the Rayleigh range equal for all the frequency components.

The effective wavelength λ_e of the pulses can be obtained from the Rayleigh range expression of a monochromatic Gaussian beam:

$$z_0\equiv\frac{\pi w_0^2}{\lambda_e}. \tag{4.6.15}$$

With use of Eq. (4.6.14) ($w_0=w_e$), we obtain

$$\lambda_e=\pi q_1. \tag{4.6.16}$$

Therefore, q_1 is related to the effective wavelength of the pulses. The far-field diffraction angle of the entire pulse also has the same mathematical form as that of a Gaussian beam. It can be obtained from Eqs. (4.6.13), (4.6.14), and (4.6.16):

$$\theta_f\equiv\frac{\rho}{z}\approx\sqrt{\frac{2q_1}{q_2}}=\frac{\lambda_e}{\pi w_e}=\frac{w_e}{z_0}. \tag{4.6.17}$$

For a weakly diffracting pulse, we require $q_1\ll q_2$, which means the effective wavelength of the pulses is much shorter than the Rayleigh range.

It can be seen that the effective wavelength of the pulse characterizes the peak wavelength in the amplitude spectrum $|\tilde{E}_y^r(\mathbf{r},\omega)|$ on axis. The maximum of this distribution occurs at the frequency $\omega_p=2c/q_1$, hence the peak wavelength of the pulse is given by $\lambda_p=\pi q_1$. Moreover, the pulse width and the peak wavelength of the pulse are related by the speed of light: $\tau_p\sim\pi q_1/c$. In fact, as shown by an accurate analysis in the previous section, the pulse width on axis is given by $2\sqrt{3}q_1/c$.

In short, the diffraction of the energy of the entire pulse is similar to that of a monochromatic Gaussian beam with an effective wavelength πq_1 that characterizes the peak wavelength in the amplitude spectrum, beam waist $\sqrt{q_1q_2/2}$, Rayleigh range $q_2/2$, and far-field diffraction angle $\sqrt{2q_1/q_2}$. The real and the imaginary pulses have the same diffraction behavior. From Eq. (4.6.11), the highest energy density is along the propagation axis ($\rho=0$). This value is proportional to the fifth power of the effective frequency.

In the limit $q_1\ll q_2$, the pulse energy passing through each transverse plane is given by the integration of Eq. (4.6.11) over the whole plane, which yields the electromagnetic energy of the pulse

$$U_{\mathrm{EM}}=\int\int_{\mathbf{s}}\Gamma(\mathbf{r})ds=\frac{3f_0^2\pi^2\mu_0}{16q_2q_1^4}. \tag{4.6.18}$$

As expected, this quantity is independent of the propagation distance z. This is the result of energy conservation when the pulse propagates in space. Note that Eq. (4.6.18) equals the first term in the exact electromagnetic energy expression (3.6).

Figure 11 is plotted from Eq. (4.6.11) to show the distribution of the pulse energy on the transverse planes at the focus ($z=0$) and in the far field ($z=20$ cm). The pulse spread due to the propagation is clearly observed. Figure 12 is generated from Eq. (4.6.12) to demonstrate the diffraction of the entire pulse. It is similar to that of a monochromatic Gaussian beam.

G. Off-axis spectral shift

Because the pulse solution is inherently nonseparable, the amplitude spectrum, and hence the pulse shape, will depend

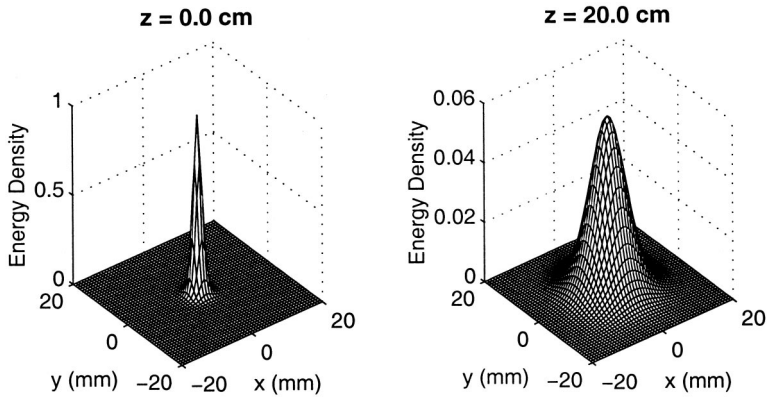

FIG. 11. Energy density on two transverse planes. (a) $z=0$ cm. (b) $z=20$ cm. The plots are normalized by the peak value of the energy density at the focus.

on both ρ and z. The spectral analysis reveals that each frequency component of the pulses propagates independently as a conventional Gaussian beam with the same Rayleigh range but with different beam waists proportional to $\sqrt{\lambda}$. Thus, in the near field, high frequency beams are more tightly confined about the propagation axis. The fact that all the frequency components have the same Rayleigh range results in an invariance of the spectra on axis. On the other hand, the frequency dispersion of the beam waist causes a redshift and reduced FWHM bandwidth of the spectra off axis. Figure 13 shows the off-axis spectral shift.

In the limit $q_1 \ll q_2$, the spatially resolved amplitude spectrum is given by

$$|\tilde{E}_y^r(\mathbf{r},\omega)| \propto \frac{\omega^2}{\sqrt{4z^2+q_2^2}} \exp\left\{-\left(\frac{q_1}{c}+\frac{q_2}{c}\frac{\rho^2}{4z^2+q_2^2}\right)|\omega|\right\}. \tag{4.7.1}$$

This equation represents the amplitude spectra on transverse planes at different propagation distances. Taking a derivative of the above equation, the peak frequencies in the spectra are obtained. They are

$$\nu_p(\mathbf{r}) = \frac{c}{\pi q_1}\frac{1}{\left\{1+\dfrac{\rho^2}{2w^2(z)}\right\}}. \tag{4.7.2}$$

The FWHM bandwidths are given by

$$\Delta\nu_{\mathrm{FWHM}}(\mathbf{r}) \approx 1.6973\nu_p(\mathbf{r}) = \frac{0.5403c}{q_1}\frac{1}{\left\{1+\dfrac{\rho^2}{2w^2(z)}\right\}}. \tag{4.7.3}$$

As shown in Eqs. (4.7.2) and (4.7.3), the highest peak frequency and broadest bandwidth occur on axis ($\rho=0$). This peak frequency and FWHM bandwidth are independent of the propagation distance z, therefore the spectrum on axis is invariant during the propagation. Equations (4.7.2) and (4.7.3) support the discussion in Sec. IV C about the pulse width [see Eq. (4.3.8)]. This result confirms the arguments in the last section. That is, the same Rayleigh range for all the frequencies results in an invariance of the spectrum on axis.

On the other hand, for a fixed distance z, the peak frequencies and FWHM bandwidths decrease with increasing ρ, therefore the off-axis spectra have a redshift and the FWHM bandwidth is reduced by a factor of $\{1+\rho^2/2w^2(z)\}$. As shown in the previous section [see Eq. (4.3.8)], the pulse width off axis is increased by the same factor as the result of this bandwidth reduction. In the near field the high frequency components are more concentrated about the axis, and are gradually lost with increasing ρ, so the longer wavelength begins to dominate the spectrum. Combining Eq. (4.3.8) with Eq. (4.7.3), we have

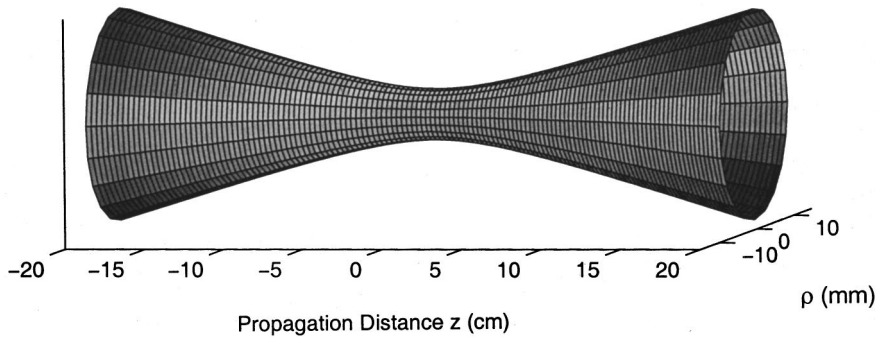

FIG. 12. A plot of energy surface to demonstrate the diffraction of the entire pulse during the propagation. This surface is defined by the criterion e^{-2} for the ratio of the energy at the beam edges to that at the beam center. The pulse energy diffracts as a monochromatic Gaussian beam with an effective wavelength πq_1.

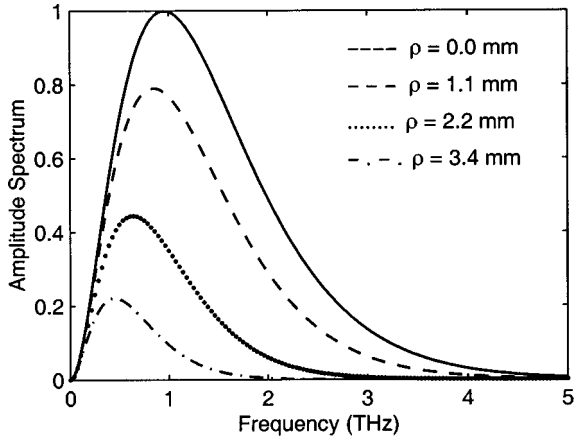

FIG. 13. Off-axis spectral shift for fixed propagation distance z. The spectra are normalized by the peak value of the spectrum on axis ($\rho=0$). Both peak frequency and bandwidth are downshift as ρ increases.

$$\Delta\nu_{\mathrm{FWHM}}(\mathbf{r})\,\tau_p(\mathbf{r})\approx 1.87. \tag{4.7.4}$$

As expected, the time-bandwidth product is constant anywhere in space and time, and is independent of q_1 and q_2. This value of time-bandwidth product characterizes single-cycle pulses.

Equation (4.7.3) implies an interesting feature of the single-cycle pulses. The peak frequency and the bandwidth of the pulse are not independent. If one of them is chosen, the other is also fixed. This differs from standard models of pulse propagation that involve a temporal envelope multiplied by a carrier frequency. In that model, the carrier frequency and the envelope width, which determines the bandwidth of the pulse, are given independently.

H. Power spectrum and amplitude spectrum

The power spectrum of the pulses is derived by integration of Eq. (4.6.1) over the cross section of the beam. Using cylindrical coordinate, the power spectrum can be calculated from

$$S(\omega)=\frac{c\varepsilon_0}{2\pi}\int\int_s|\tilde{E}_y^r(\mathbf{r},\omega)|^2\rho\,d\rho\,d\varphi, \tag{4.8.1}$$

which yields

$$S(\omega)=\frac{f_0^2\pi^2\mu_0|\omega|^3}{4c^4q_2}\exp\left\{-\frac{2|\omega|}{c}q_1\right\},\quad -\infty<\omega<+\infty. \tag{4.8.2}$$

This expression satisfies the general property of the power spectrum, i.e., $S(\omega)=S(-\omega)$. The real and imaginary pulses have the same power spectrum. Note the integration of Eq. (4.8.2) over the whole spectrum yields Eq. (4.6.18), the pulse energy in the limit $q_1\ll q_2$. The frequency of the intensity peak in the power spectrum is $\nu_p=3c/(4\pi q_1)$, or in terms of wavelength, $\lambda_p=4\pi q_1/3\approx 4q_1$. Figure 14 plots the power spectrum of the pulses.

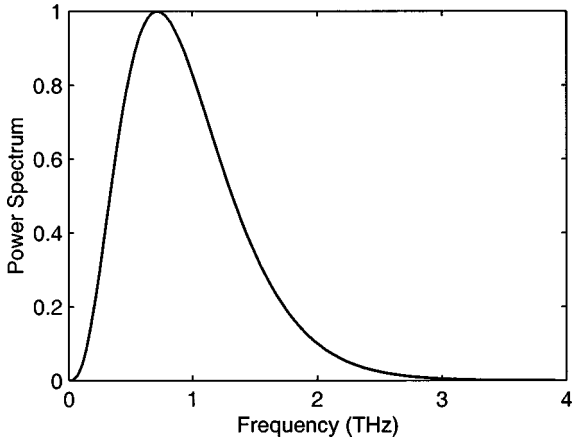

FIG. 14. Power spectrum of the pulse.

The cutoff frequency ω_c of the power spectrum can be computed by defining it as the (angular) frequency above which the power spectrum contains the fraction η of the total energy:

$$\eta=\frac{\int_{\omega_c}^{\infty}S(\omega)d\omega}{\int_0^{\infty}S(\omega)d\omega}. \tag{4.8.3}$$

This yields

$$\eta=\{1+\gamma+\tfrac{1}{2}\gamma^2+\tfrac{1}{6}\gamma^3\}\exp(-\gamma), \tag{4.8.4}$$

where $\gamma\equiv 2q_1\omega_c/c=4\pi q_1/\lambda_c$. The cutoff frequency of the pulses can be calculated from this expression. For example, the cutoff frequency is given by $\gamma=10.045$ for $\eta=0.01$; that is, $\lambda_c=1.25q_1$; and by $\gamma=4\pi$ for $\eta=0.0015$, that is, $\lambda_c=q_1$. Thus q_1 equals the cutoff wavelength of the pulse.

In terahertz experiments, the electric field is measured directly, so the amplitude spectrum is more relevant. The amplitude spectrum can be defined by

$$|\tilde{E}_y^r(\omega)|\equiv\sqrt{S(\omega)}\propto|\omega|^{3/2}\exp\left\{-\frac{q_1}{c}|\omega|\right\}. \tag{4.8.5}$$

This type of a power term multiplied by an exponential term is a typical shape of amplitude spectrum in terahertz experiments.

V. PHYSICAL REALIZATION

The question that still remains is this: how does one generate these solutions, at least approximately, in the laboratory? In this section we show that these pulse solutions are natural spatiotemporal modes of a cavity resonator. As such they should be realizable by exciting a curved mirror resonator or the equivalent lens waveguide.

There are three key insights that lead us to propose the resonant cavity scheme for generating these solutions. First, as shown in Sec. IV F, the Fourier spectrum of these pulses consists of an ensemble of Gaussian beams of different frequencies all of which have the same Rayleigh range z_0 and radius of curvature $R(z)$. One way to enforce this condition

is through the use of a resonator consisting of two curved mirrors of radii of curvature R_1 and R_2 separated by a distance L. For a symmetric resonator with $R_1=R_2$, the minimum spot size of the modes occurs at the center of the cavity and is given by

$$w_0^2=\frac{\lambda}{2\pi}\sqrt{L(2R-L)}.$$

The confocal parameter is given by

$$b=2z_0\equiv\frac{2\pi w_0^2}{\lambda}=\sqrt{L(2R-L)}.$$

Once the mirror separation and radii of curvature have been specified, the confocal parameter is fixed. The beam waists will scale so that $w_0^2\propto\lambda$, thus keeping b fixed. This single confocal parameter characterizes the whole pulse as well as its frequency components. It is also clear that specifying the confocal parameter determines the wave front radius of curvature $R(z)=z\{1+(z_0/z)^2\}$ for all the frequency components as well as for the entire pulse. Placing mirrors of the appropriate radii of curvature at positions where they match the pulse front curvature will ensure that the solution matches the boundary conditions at the mirrors. Finally, in order to ensure that the temporal profile of the generated pulse matches that of the solutions, the pulse must reproduce itself in space and time after a number of round trips in the cavity. In other words, it should be a spatiotemporal mode of the resonator. That possibility is ensured by the symmetry of the solutions under time reversal and space inversion, Eq. (4.3.7).

To test this idea we follow a pulse solution as it evolves inside a confocal resonator. The pulse length is much shorter than the transit time in the cavity (ensured by the condition $q_1\ll q_2$). Starting from an arbitrary reference plane (say, plane B at $z=0$) with an initial pulse $E_y^r(z=0,\rho,T)$ propagation to the right mirror adds a phase $\phi(R/2)=\tan^{-1}(1)=\pi/4$ which transforms the shape of the pulse. The mirror's radius of curvature matches that of the pulse and its aperture is sufficiently large that diffraction effects are negligible. Reflection at the right mirror imparts a π phase shift and hence an inverted and transformed pulse propagates back toward the center. Upon propagation to the left mirror, reflection, and propagation back to the $z=0$ reference plane, the pulse is identical in spatial and temporal profile to the initial one. However, its polarity is reversed. After a second round trip the final pulse is identical to the initial one. Similar considerations lead to another spatiotemporal mode described by $E_y^i(\mathbf{r},T)$. The key point is that the confocal placement of mirrors whose radii of curvature match those of the pulse that satisfies Maxwell's equations and the boundary conditions.

In a practical experiment the pulse source may be located either inside or outside the cavity. A pulse from an external source can be matched fairly closely to the fundamental transverse mode of the cavity using mode-matching optics. The match need not be exact. After a few round trips, the pulse will settle into a self-reproducing mode. The output will then consist of a train of eigenpulses separated by the cavity round trip time. The pulse train will have an envelope that decays exponentially at a rate determined by the cavity Q.

VI. CONCLUSION

In conclusion, we have presented exact solutions of Maxwell's equations that describe the spatiotemporal evolution of focused single-cycle pulses. These solutions are spatiotemporal modes of single-cycle pulses in a confocal resonator. In contrast to previous formulations we used a Hertz vector oriented transversely to the propagation direction. The resulting pulse solutions have finite total energy. Our energy expression, however, differs from that of Ziolkowski's EDEPT solution by some additional terms that arise from the breakdown of axial symmetry of the resulting electromagnetic fields. We elucidate the role of the Gouy phase shift in causing polarity reversals and temporal reshaping as these pulses evolve through the focus. A physical realization of these pulses in a confocal resonator scheme has been proposed.

Finally, the bandwidth and the peak frequency are not independent for these single-cycle pulses. The higher the frequency, the broader the bandwidth, thus the shorter the pulse width. Therefore, ultrashort single-cycle optical pulses are likely to be generated by going to extremely short wavelengths.

A set of useful and simple formulas has been developed in this paper. These formulas were derived from the exact solutions of Maxwell's equations. They are capable of describing focused single-cycle electromagnetic pulses, hence can be used in experiments as a set of working equations to calculate the parameters of single-cycle pulses. These equations are all related to the parameters q_1 and q_2 which describe, respectively, the wavelength and Rayleigh range of the pulses. By measuring any two independent quantities of the pulse to determine the values of q_1 and q_2, all the other quantities can be calculated by using this set of equations, which are listed here for convenience.

Beam waist of each frequency	$w_0^2=\frac{\lambda q_2}{2\pi}$
Effective beam waist of entire pulse	$w_e^2=\frac{1}{2}q_1q_2$
Rayleigh range	$z_0=\frac{1}{2}q_2$
Far-field diffraction angle of each frequency	$\theta_f=\sqrt{\frac{2\lambda}{\pi q_2}}$
Far-field diffraction angle of entire pulse	$\theta_f=\sqrt{\frac{2q_1}{q_2}}$
Cutoff wavelength	$\lambda_c=q_1$
Effective wavelength	$\lambda_e=\pi q_1$
Peak frequency*	$\nu_p(\mathbf{r})=\frac{c}{\lambda_e a(\mathbf{r})}$
Bandwidth*	$\Delta\nu_{\mathrm{FWHM}}(\mathbf{r})\approx\frac{0.54c}{q_1 a(\mathbf{r})}$

Pulse width*	$\tau_p(\mathbf{r})=2\sqrt{3}\,\frac{q_1 a(\mathbf{r})}{c}$
Time-bandwidth product	$\Delta\nu_{\mathrm{FWHM}}(\mathbf{r})\,\tau_p(\mathbf{r})\approx 1.87$
Relation between $\Delta\nu_{\mathrm{FWHM}}$and ν_p	$\Delta\nu_{\mathrm{FWHM}}(\mathbf{r})\approx 1.7\nu_p(\mathbf{r})$
Group velocity [13]	$\frac{\nu_g}{c}=1-\frac{2q_1}{3q_2}$
Amplitude spectrum	$\lvert\tilde{E}(\omega)\rvert\propto\omega^{3/2}\exp\left\{-\frac{q_1}{c}\omega\right\}$
Temporal waveform of complex field	$A(T)\exp\{i[\alpha(T)+\phi(z)]\}$
$A(T)\propto(1+T^2)^{-3/2}$	
$\alpha(T)=3\tan^{-1}(T)$	
$\phi(z)=\tan^{-1}(z/z_0)$	
Dimensionless scaled local time	$T=\frac{ct-z-\rho^2/2R}{q_1 a(\mathbf{r})}$
*Scaling parameter	$a(\mathbf{r})=1+\frac{\rho^2}{2w^2(z)}$
*Beam size	$w^2(z)=w_e^2\left\{1+\left(\frac{z}{z_0}\right)^2\right\}$

ACKNOWLEDGMENT

This research was partially supported by the National Science Foundation through the Center for Ultrafast Optical Science under Grant No. STC PHY 8920108 and by the U.S. Air Force Office of Scientific Research.

APPENDIX A

From the following discussion, it will be seen that the two poles in Eq. (2.15) are always in the lower half-plane no matter what the values of ρ and z. Hence the fields and the generating function are analytical functions of time at any spatial point $\mathbf{r}$.

For any point on axis ($\rho=0$), the poles are given by

$$ct_1=-z-iq_2,\quad ct_2=z-iq_1,\quad (q_1,q_2>0) \tag{A1}$$

The imaginary part of Eq. (A1) are independent of z. For the points off axis, let

$$\beta\equiv\sqrt{\left(z+i\frac{q_2-q_1}{2}\right)^2+\rho^2}=\beta_r+i\beta_i.$$

Square both sides of above equation,

$$\beta_r^2-\beta_i^2=z^2-\frac{(q_2-q_1)^2}{4}+\rho^2,$$

$$2\beta_r\beta_i=z(q_2-q_1). \tag{A2}$$

For any fixed value z, to satisfy both equations in Eq. (A2), when ρ increases, $|\beta_r|$ will increase, and simultaneously $|\beta_i|$ will decrease. So $|\beta_i|$ is maxim on axis, and always decreases as increasing ρ. The maximum value of $|\beta_i|$ is given by $|q_2-q_1|/2$. When $\rho\to\infty$, $|\beta_i|\to 0$, and $ct_1=ct_2=-i(q_1+q_2)/2$.

Therefore, the imaginary parts of the poles are negative and independent of z for any point on axis. When ρ increases, the imaginary parts of the poles will approach to each other, and end up with the same value $-(q_1+q_2)/2$ as $\rho\to\infty$.

APPENDIX B

In this appendix, we will show that for a transverse construction of the Hertz vector, the EDEPT solutions will have finite electromagnetic energy, i.e., Eqs. (3.1), if spectrum $k^{3/2}F(k)$ is square integrable.

The electromagnetic energy expression associated with the x-oriented Hertz vector is given by

$$U_{\mathrm{EM}}=\frac{1}{2}\int_{-\infty}^{+\infty}dz\int_0^{+\infty}\rho\,d\rho\int_0^{2\pi}d\varphi(\varepsilon_0|E_y|^2+\varepsilon_0|E_z|^2+\mu_0|H_x|^2+\mu_0|H_y|^2+\mu_0|H_z|^2). \tag{B1}$$

Applying the operators in Eqs. (2.8) and (2.9) directly to Eq. (2.2), we obtain the expansions of the field components over spectrum $F(k)$:

$$\begin{aligned}
E_y(\mathbf{r},t)&=\int_0^{+\infty}dk\,F(k)\tilde{E}_y(\mathbf{r},t,k),\\
E_z(\mathbf{r},t)&=\int_0^{+\infty}dk\,F(k)\tilde{E}_z(\mathbf{r},t,k),\\
H_x(\mathbf{r},t)&=\int_0^{+\infty}dk\,F(k)\tilde{H}_x(\mathbf{r},t,k),\\
H_y(\mathbf{r},t)&=\int_0^{+\infty}dk\,F(k)\tilde{H}_y(\mathbf{r},t,k),\\
H_z(\mathbf{r},t)&=\int_0^{+\infty}dk\,F(k)\tilde{H}_z(\mathbf{r},t,k),
\end{aligned} \tag{B2}$$

where

$$\tilde{E}_y(\mathbf{r},t,k)=-\mu_0 c e^{-ks}\left\{\frac{k^2\rho^4}{(q_1+i\tau)^5}-\frac{4k\rho^2}{(q_1+i\tau)^4}+\frac{2}{(q_1+i\tau)^3}-\frac{k^2}{(q_1+i\tau)}\right\}, \tag{B3}$$

$$\tilde{E}_z(\mathbf{r},t,k)=i2\mu_0 c e^{-ks}\left\{\frac{k^2\rho^3}{(q_1+i\tau)^4}-\frac{2k\rho}{(q_1+i\tau)^3}-\frac{k^2\rho}{(q_1+i\tau)^2}\right\}\sin\varphi, \tag{B4}$$

$$\tilde{H}_x(\mathbf{r},t,k)=e^{-ks}\left\{\frac{k^2\rho^4}{(q_1+i\tau)^5}-\frac{4k\rho^2}{(q_1+i\tau)^4}+\frac{2}{(q_1+i\tau)^3}+\frac{2k^2\rho^2\cos 2\varphi}{(q_1+i\tau)^3}+\frac{k^2}{(q_1+i\tau)}\right\}, \tag{B5}$$

$$\tilde{H}_y(\mathbf{r},t,k)=e^{-ks}\frac{2k^2\rho^2}{(q_1+i\tau)^3}\sin 2\varphi, \tag{B6}$$

$$\tilde{H}_z(\mathbf{r},t,k)=-i2e^{-ks}\left\{\frac{k^2\rho^3}{(q_1+i\tau)^4}-\frac{2k\rho}{(q_1+i\tau)^3}+\frac{k^2\rho}{(q_1+i\tau)^2}\right\}\cos\varphi, \tag{B7}$$

where

$$s=\frac{\rho^2}{q_1+i\tau}-i\sigma,$$

With use of Eq. (B2), the energy expression (B1) becomes

$$U_{\mathrm{EM}}=\frac{1}{2}\int_0^\infty\int_0^\infty dk\,dk'\,F(k)F^*(k')\int_{-\infty}^{+\infty}dz\int_0^\infty\rho\,d\rho\int_0^{2\pi}d\varphi\times\{\varepsilon_0\tilde{E}_y(k)\tilde{E}_y^*(k')+\varepsilon_0\tilde{E}_z(k)\tilde{E}_z^*(k')+\mu_0\tilde{H}_x(k)\tilde{H}_x^*(k')+\mu_0\tilde{H}_y(k)\tilde{H}_y^*(k')+\mu_0\tilde{H}_z(k)\tilde{H}_z^*(k')\}. \tag{B8}$$

Apparently there are 60 terms that need to be calculated in substituting Eqs. (B3)–(B7) into Eq. (B8). By grouping terms properly, before carrying on the calculations many terms can be dropped either due to cancellation or due to angular integration. Hence the calculation task is greatly reduced to 17 terms. With the substitution of those 17 terms into Eq. (B8), we have

$$U_{\mathrm{EM}}=2\pi\mu_0\int_0^\infty\int_0^\infty dk\,dk'F(k)F^*(k')\times\int_{-\infty}^{+\infty}dz\int_0^\infty\rho\,d\rho\,e^{-ks-k's^*}\times\left\{AB+2CD+\frac{k^2k'^2}{(q_1^2+\tau^2)}+\frac{2k^2k'^2\rho^4}{(q_1^2+\tau^2)^3}+\frac{2k^2k'^2\rho^2}{(q_1^2+\tau^2)^2}\right\}, \tag{B9}$$

where

$$A(k)=\frac{k^2\rho^4}{(q_1+i\tau)^5}-\frac{4k\rho^2}{(q_1+i\tau)^4}+\frac{2}{(q_1+i\tau)^3},\quad B=A^*(k'),$$
$$C(k)=\frac{k^2\rho^3}{(q_1+i\tau)^4}-\frac{2k\rho}{(q_1+i\tau)^3},\quad D=C^*(k'). \tag{B10}$$

After the ρ integrations and some algebraic manipulations one obtains

$$U_{\mathrm{EM}}=2\pi\mu_0\int_0^\infty\int_0^\infty dk\,dk'F(k)F^*(k')k^2k'^2\times\int_{-\infty}^{+\infty}dz e^{-i(k'-k)\sigma}\left\{\frac{24}{\alpha^5}+\frac{4}{\alpha^3}+\frac{12}{\alpha^4}+\frac{2}{\alpha^2}+\frac{1}{\alpha}\right\}, \tag{B11}$$

where

$$\alpha\equiv(k'+k)q_1+i(k'-k)\tau. \tag{B12}$$

The z integration is performed with use of the following expression developed by Ziolkowski [3],

$$\int_{-\infty}^{+\infty}dy\frac{e^{-ixy}}{(\Lambda+ixy)^m}=2\pi\delta(x)\,\frac{e^\Lambda}{\Lambda^{m-1}}E_m(\Lambda),$$

where

$$E_m(\Lambda)\equiv\int_\Lambda^{+\infty}\frac{e^{-\Lambda t}}{t^m}dt.$$

With $x=k'-k$, $y=\tau$, and $\Lambda=(k'+k)q_1$, Eq. (B11) becomes

$$U_{\mathrm{EM}}=2\pi^2\mu_0\int_0^\infty dk|F(k)|^2k^4\times e^{2kq_1}\left\{\frac{24E_5(2kq_1)}{(2kq_1)^4}+\frac{12E_4(2kq_1)}{(2kq_1)^3}+\frac{4E_3(2kq_1)}{(2kq_1)^2}+\frac{2E_2(2kq_1)}{(2kq_1)}+E_1(2kq_1)\right\}. \tag{B13}$$

Using the recurrence relation

$$E_{n+1}(x)=\frac{1}{n}[e^{-x}-xE_n(x)],$$

Eq. (B13) is simplified to

$$U_{\mathrm{EM}}=\frac{3\pi^2\mu_0}{4q_1^4}\int_0^\infty dk|F(k)|^2[1+\tfrac{2}{3}(kq_1)+\tfrac{2}{3}(kq_1)^2+\tfrac{4}{3}(kq_1)^3]. \tag{B14}$$

[1] J. N. Brittingham, J. Appl. Phys. **54**, 1179 (1983).
[2] R. W. Ziolkowski, J. Math. Phys. **26**, 861 (1985).
[3] R. W. Ziolkowski, Phys. Rev. A **39**, 2005 (1989).
[4] R. W. Hellwarth and P. Nouchi, Phys. Rev. E **54**, 889 (1996).
[5] S. Feng, H. G. Winful, and R. W. Hellwarth, Opt. Lett. **23**, 385 (1998); Opt. Lett. **23**, 1141 (1998).
[6] A. Nahata and T. F. Heinz, IEEE J. Sel. Top. Quantum Electron. **2**, 701 (1996); M. Van Exter, Ch. Fattinger, and D. Grischkowsky, Appl. Phys. Lett. **55**, 337 (1989); D. Grischkowsky, S. Keiding, M. Van Exter, and Ch. Fattinger, J. Opt. Soc. Am. B **7**, 2006 (1990); P. Uhd Jepsen and S. R. Keiding, Opt. Lett. **20**, 807 (1994).
[7] D. You and P. H. Bucksbaum, J. Opt. Soc. Am. B **14**, 1651 (1997).
[8] E. Budiarto, N.-W. Pu, S. Jeong, and J. Bokor, Opt. Lett. **23**, 213 (1998).
[9] A. E. Kaplan, J. Opt. Soc. Am. B **15**, 951 (1998).
[10] Z. Wang, Z. Zhang, Z. Xu, and Q. Lin, IEEE J. Quantum Electron. **33**, 566 (1997).
[11] S. R. Keiding and D. Grischkowsky, Opt. Lett. **15**, 48 (1990).
[12] J. W. Goodman, *Introduction to Fourier Optics*, 2nd ed. (McGraw-Hill, New York, 1996), p. 54.
[13] S. Feng and H. G. Winful (unpublished).